INTERNATIONAL JOURNAL FOR NUMERICAL METHODS IN ENGINEERING
Int. J. Numer. Meth. Engng 2006; **00**:1 *Prepared using* nmeauth.cls *[Version: 2002/09/18 v2.02]*

An explicit discontinuous Galerkin method for non-linear solid dynamics. Formulation, parallel implementation and scalability properties.

L. Noels[1,2,†], R. Radovitzky[1,*]

[1] *Massachusetts Institute of Technology, Department of Aeronautics and Astronautics*
77 Massachusetts Ave, Cambridge, MA 02139-4307
[2] *University of Liège, LTAS-Milieux Continus & Thermomécanique*
Chemin des Chevreuils 1, B-4000 Liège, Belgium

SUMMARY

An explicit-dynamics spatially-discontinuous Galerkin (DG) formulation for non-linear solid dynamics is proposed and implemented for parallel computation. Discontinuous Galerkin methods have particular appeal in problems involving complex material response, e.g. non-local behavior and failure, as, even in the presence of discontinuities, they provide a rigorous means of ensuring both consistency and stability. In the proposed method, these are guaranteed: the former by the use of average numerical fluxes, and the latter by the introduction of appropriate quadratic terms in the weak formulation. The semi-discrete system of ordinary differential equations is integrated in time using a conventional second-order central-difference explicit scheme. A stability criterion for the time integration algorithm, accounting for the influence of the DG discretization stability, is derived for the equivalent linearized system. This approach naturally lends itself to efficient parallel implementation. The resulting DG computational framework is implemented in three dimensions via specialized interface elements. The versatility, robustness and scalability of the overall computational approach are all demonstrated in problems involving stress-wave propagation and large plastic deformations.

KEY WORDS: Discontinuous Galerkin method; elliptic equation; explicit time integration; non-linear dynamics

1. INTRODUCTION

Among the reasons that spatially-discontinuous Galerkin methods are attractive in the field of solid mechanics is the fact that they provide a means of enforcing (higher-order) continuity requirements in a weak manner in the solution of initial boundary value problems. In their basic form, DG methods constitute a generalization of weak formulations, allowing for discontinuities of the problem unknowns in the interior of the problem domain. This is usually accomplished

*Correspondence to: Tel: +1-617-252-1518, Fax: +1-617-253-0361, E-mail: rapa@mit.edu
†Postdoctoral Scholar at the Belgian National Fund for Scientific Research (FNRS)

Received
Revised

by integrating by parts the governing equations in subdomains: a process which naturally leads to boundary integral terms on the subdomain interfaces involving jump discontinuities. Clearly, the role of these terms is to enforce the consistency and the continuity of the problem unknowns in a weak manner, where appropriate. In the context of finite element formulations of elliptic problems, jump-discontinuities are allowed across element boundaries.

Recent efforts to exploit the advantages of DG methods in solid mechanics have included applications to linear [1] and nearly-incompressible elasticity [2], beams and plates [3], shells [4], failure [5] and strain-gradient theories of damage [6, 7]. Formulations applicable to the nonlinear theory of large elastic deformation of solids have recently emerged [8, 9]. In [9], a general discontinuous Galerkin formulation for finite elasticity based on the three-field Hu-Washizu-de Veubeke functional for large deformations was proposed. The resulting variational statement [9] leads naturally to the formulation of average stress fluxes at interelement boundaries which guarantee consistency, while stability is ensured by a (sufficiently large) quadratic term. The integration of the interelement boundary consistency and stability terms is implemented within the framework of interface elements for simplicity and for compatibility with existing code. In both references [8, 9], implementations and examples of application in three dimensions were provided, thus demonstrating the feasibility, accuracy and versatility of the methods proposed. However, these formulations were restricted to nonlinear elastostatics.

The purpose of this paper is to extend the spatially-discontinuous Galerkin formulation proposed in [9] to non-linear dynamics. The integration of the equations of motion in time is achieved via a conventional central-difference explicit scheme, which is highly scalable and particularly well-suited to problems involving high deformation rates. Time integration stability is shown to require a modified CFL condition that depends on the discontinuous Galerkin stabilization parameter. In addition, modifications of the discontinuous Galerkin formulation required in the presence of plasticity are discussed. A numerical implementation using interface elements leads to a highly-efficient parallelization of the method. Numerical examples involving wave propagation, high deformation rates and plasticity are conducted to demonstrate the robustness, accuracy and scalability of the proposed formulation.

The outline of the paper is as follows: in section 2, we develop from a weak statement of the continuum dynamics equations, the space-discontinuous Galerkin formulation for large dynamic deformations. The static forces resulting from this formulation are the same as those obtained from the three-field Hu-Washizu-de Veubeke functional [9]. It follows that the spatial discretization inherits the consistency, stability and convergence rate of the formulation proposed in this reference. In section 3, the explicit time integration of the resulting differential equations is described, and the stability criterion is derived from a spectral study of the linearized equations. The parallel implementation of the method within a conventional finite-element code via interface elements is detailed in section 4. This section includes a brief discussion of its scalability properties. Section 5 is devoted to the presentation of numerical examples.

2. FORMULATION OF THE DISCONTINUOUS GALERKIN METHOD FOR SOLID DYNAMICS

We consider the dynamic motion of a body which, in its reference configuration at time $t = t_0$, occupies the region of space $B_0 \subset \mathbb{R}^3$. The configuration of the body at any time t in the

interval $\mathrm{T} = [t_0, t_f]$ can be described by the deformation mapping

$$\boldsymbol{x} = \boldsymbol{\varphi}(\boldsymbol{X}, t) \in \mathrm{H}^1(B_0) \;\; \forall \boldsymbol{X} \in B_0, \;\; \forall t \in \mathrm{T}\,, \tag{1}$$

where $\boldsymbol{x}$ is the position of the material particle $\boldsymbol{X}$. The deformation gradient characterizing the local state of deformation is defined by

$$\boldsymbol{F} = \boldsymbol{\nabla}_0 \boldsymbol{\varphi}(\boldsymbol{X}, t) \;\; \forall \boldsymbol{X} \in B_0, \;\; \forall t \in \mathrm{T}\,, \tag{2}$$

where $\boldsymbol{\nabla}_0$ is the material gradient operator and

$$J = \det(\boldsymbol{F}) > 0 \;\; \forall \boldsymbol{X} \in B_0, \;\; \forall t \in \mathrm{T}\,, \tag{3}$$

is the Jacobian of the deformation. The body is subjected to a force per unit mass $\boldsymbol{B}$ and its boundary surface ∂B_0 is partitioned into a Dirichlet portion $\partial_D B_0$ constrained by displacements $\bar{\boldsymbol{\varphi}}$ and a Neumann part $\partial_N B_0$ subjected to surface traction $\bar{\boldsymbol{T}}$. One always has $\partial B_0 = \partial_N B_0 \cup \partial_D B_0$ and $\partial_D B_0 \cap \partial_N B_0 = \emptyset$. The continuum equations stated in material form are

$$\rho_0 \ddot{\boldsymbol{\varphi}} = \boldsymbol{\nabla}_0 \cdot \boldsymbol{P} + \rho_0 \boldsymbol{B} \quad \forall \boldsymbol{X} \in B_0, \;\; \forall t \in \mathrm{T}, \tag{4}$$

$$\boldsymbol{\varphi} = \bar{\boldsymbol{\varphi}} \quad \forall \boldsymbol{X} \in \partial_D B_0, \;\; \forall t \in \mathrm{T}, \tag{5}$$

$$\boldsymbol{P} \cdot \boldsymbol{N} = \bar{\boldsymbol{T}} \quad \forall \boldsymbol{X} \in \partial_N B_0, \;\; \forall t \in \mathrm{T}, \tag{6}$$

where $\rho_0 : B_0 \to \mathbb{R}_+$ is the initial density, $\dot{\bullet}$ represents the partial differentiation with respect to time at fixed $\boldsymbol{X}$, $\boldsymbol{P} \in \left[\mathrm{H}^1(B_0)\right]^2$ is the first Piola-Kirchhoff stress tensor, $\boldsymbol{N}$ is the unit surface normal in the reference configuration, and the notation $\left[\mathrm{H}^1(B_0)\right]^2$ refers to second order tensors. In order to integrate this system of equations, displacement and velocity initial conditions

$$\boldsymbol{\varphi}(\boldsymbol{X}, t_0) = \boldsymbol{X} \quad \forall \boldsymbol{X} \in B_0, \tag{7}$$

$$\dot{\boldsymbol{\varphi}}(\boldsymbol{X}, t_0) = \dot{\boldsymbol{\varphi}}_0 \quad \forall \boldsymbol{X} \in B_0, \tag{8}$$

must be provided. We seek to develop DG formulations suitable for a large class of models of material behavior. As a step toward this end, we adopt the variational constitutive framework in [10, 11]. The advantages of the variational formulation of constitutive updates have been discussed in detail in these references. Such advantages have been exploited in the formulation of a variety of material models, including models of finite-deformation isotropic plasticity and single-crystal plasticity [11], non-cohesive granular media [12], porous plasticity [13], kidney tissue response to shocks [14], nonlinear viscoelasticity [15] and grain boundary deformation mechanisms in polycrystals [16]. This framework has recently been extended to the coupled thermomechanical response of general dissipative solids [17]. In what follows, we briefly summarize the variational approach to the formulation of constitutive updates. For conciseness, we restrict our attention to the case of large-deformation isotropic plasticity. A conventional multiplicative decomposition of the deformation gradient $\boldsymbol{F} = \boldsymbol{F}^e \boldsymbol{F}^p$ into an elastic part $\boldsymbol{F}^e$ and a plastic part $\boldsymbol{F}^p$ is assumed. The existence of a Helmholtz free energy density per unit undeformed volume

$$A(\boldsymbol{F}, \boldsymbol{F}^p, T, \boldsymbol{Q}) = W^e(\boldsymbol{F}^e, T) + W^p(\boldsymbol{F}^p, \boldsymbol{Q}, T), \tag{9}$$

where W^e is the elastic strain energy density, T is the absolute temperature, W^p the stored energy of cold work, and $\boldsymbol{Q} \in \mathbb{R}^N$ a suitable set of internal variables describing local inelastic processes is postulated. The first Piola-Kirchhoff stress tensor and the conjugate forces follow from Coleman's relations as

$$\boldsymbol{P} = \frac{\partial A}{\partial \boldsymbol{F}},\ \boldsymbol{T} = -\frac{\partial A}{\partial \boldsymbol{F}^p},\ \boldsymbol{Y} = -\frac{\partial A}{\partial \boldsymbol{Q}}\ . \tag{10}$$

The evolution of the internal variables is assumed to be governed by local kinetic equations of the implicit form

$$\boldsymbol{T} = \frac{\partial \psi^*}{\partial \dot{\boldsymbol{F}}^p}(\dot{\boldsymbol{F}}^p, \dot{\boldsymbol{Q}}),\quad \boldsymbol{Y} = \frac{\partial \psi^*}{\partial \dot{\boldsymbol{Q}}}(\dot{\boldsymbol{F}}^p, \dot{\boldsymbol{Q}}), \tag{11}$$

where $\psi^*(\dot{\boldsymbol{F}}^p, \dot{\boldsymbol{Q}})$ is a (dual) inelastic potential. The variational structure of the constitutive framework then follows from the definition of the rate potential:

$$D(\dot{\boldsymbol{F}}, \dot{\boldsymbol{F}}^p, \dot{\boldsymbol{Q}}) = \frac{\partial A}{\partial \boldsymbol{F}} \cdot \dot{\boldsymbol{F}} + \frac{\partial A}{\partial \boldsymbol{F}^p} \cdot \dot{\boldsymbol{F}}^p + \frac{\partial A}{\partial \boldsymbol{Q}} \cdot \dot{\boldsymbol{Q}} + \psi^*(\dot{\boldsymbol{F}}^p, \dot{\boldsymbol{Q}})\ . \tag{12}$$

as its stationary points satisfy the constitutive equation for the stress (10) and give the values $\dot{\boldsymbol{F}}^{p*}, \dot{\boldsymbol{Q}}^*$ satisfying the constraints

$$\frac{\partial A}{\partial \boldsymbol{F}^p} + \frac{\partial \psi^*}{\partial \dot{\boldsymbol{F}}^p} = 0,\quad \frac{\partial A}{\partial \boldsymbol{Q}} + \frac{\partial \psi^*}{\partial \dot{\boldsymbol{Q}}} = 0 \tag{13}$$

arising from (10) and (11). Alternatively, the effective potential defined as

$$D_{\text{eff}}(\dot{\boldsymbol{F}}) = \min_{\dot{\boldsymbol{F}}^p, \dot{\boldsymbol{Q}}} \left\{ \frac{\partial A}{\partial \boldsymbol{F}} \cdot \dot{\boldsymbol{F}} + \frac{\partial A}{\partial \boldsymbol{F}^p} \cdot \dot{\boldsymbol{F}}^p + \frac{\partial A}{\partial \boldsymbol{Q}} \cdot \dot{\boldsymbol{Q}} + \psi^*(\dot{\boldsymbol{F}}^p, \dot{\boldsymbol{Q}}) \right\} \tag{14}$$

plays the role of a rate potential for the stresses, since it follows directly that:

$$\boldsymbol{P} = \frac{\partial D_{\text{eff}}}{\partial \dot{\boldsymbol{F}}}. \tag{15}$$

The large deformation plasticity model used in this work to illustrate the DG formulation in the context of nonlinear, history-dependent material behavior is based on this variational framework. Specific details of the model and the incremental constitutive integration algorithm are provided in Appendix I.

2.1. Discontinuous Galerkin discretization

A finite element discretization $B_{0h} = \bigcup_{e=1}^{E} \bar{\Omega}_0^e$, where $\bar{\Omega}_0^e$ is the union of the open domain Ω_0^e with its boundary $\partial\Omega_0^e$, of the reference configuration B_0 is considered, with

$$\begin{aligned}
\partial\Omega_0^e &= \partial_D\Omega_0^e \cup \partial_N\Omega_0^e \cup \partial_I\Omega_0^e\ , \\
\partial_D\Omega_0^e &= \partial\Omega_0^e \cap \partial_D B_{0h}\ , \\
\partial_N\Omega_0^e &= \partial\Omega_0^e \cap \partial_N B_{0h}\ , \\
\partial_I B_{0h} &= \left[\bigcup_{e=1}^{E} \partial\Omega_0^e\right] \backslash \partial B_{0h}\ ,
\end{aligned} \tag{16}$$

where subscript I is used to refer to the boundary between the elements. A finite-dimensional piecewise polynomial approximation $\boldsymbol{\varphi}_h$, $\boldsymbol{P}_h$ of the solution is defined in the spaces

$$\mathrm{X}_{\mathrm{h}}^{k} = \left\{ \boldsymbol{\varphi}_{\mathrm{h}} \in \mathrm{L}^2\left(B_{0h}\right) | \left[\boldsymbol{\varphi}_{\mathrm{h}}|_{\Omega_0^e} \in \mathbb{P}^k\left(\Omega_0^e\right) \ \forall \Omega_0^e \in B_{0h} \right] \right\} \subset \mathrm{X}^{\mathrm{f}}\left(B_{0h}\right) = \prod_e \left(\mathrm{H}^1(\Omega_0^e) \right) \ , \tag{17}$$

$$\mathrm{S}_{\mathrm{h}}^{k} = \left\{ \boldsymbol{P}_{\mathrm{h}} \in \left[\mathrm{L}^2\left(B_{0h}\right)\right]^2 | \left[\boldsymbol{P}_{\mathrm{h}}|_{\Omega_0^e} \in \mathbb{P}^k\left(\Omega_0^e\right)^2 \ \forall \Omega_0^e \in B_{0h} \right] \right\} \subset \mathrm{S}^{\mathrm{f}}\left(B_{0h}\right) = \prod_e \left(\left[\mathrm{H}^1(\Omega_0^e)\right]^2 \right), \tag{18}$$

where $\mathbb{P}^k\left(\Omega_0^e\right)$ is the set of polynomial functions up to degree $k \geq 1$. Let $\delta\boldsymbol{\varphi}_h \in \mathrm{X}_{\mathrm{hc}}^{k}$ be an arbitrary test function defined in the space

$$\begin{aligned} \mathrm{X}_{\mathrm{hc}}^{k} \quad = \quad & \left\{ \delta\boldsymbol{\varphi}_h \in \mathrm{X}_{\mathrm{h}}^{k} | [\delta\boldsymbol{\varphi}_h = 0 \ \forall \boldsymbol{X} \in \partial_D B_{0h}, \ \forall t \in \mathrm{T} \text{ and } \delta\boldsymbol{\varphi}_h\left(t_0\right) = 0 \ \forall \boldsymbol{X} \in B_{0h} \right. \\ & \left. \text{and } \delta\boldsymbol{\varphi}_h\left(t_f\right) = 0 \ \forall \boldsymbol{X} \in B_{0h}] \right\} \ . \end{aligned} \tag{19}$$

Integration over the body in the reference configuration of Eq. (4) multiplied by this test function leads to a weak formulation of the problem, which consists of finding $\boldsymbol{\varphi} \in \mathrm{X}_{\mathrm{h}}^{k}$ and $\boldsymbol{P}_h \in \mathrm{S}_{\mathrm{h}}^{k}$ such that

$$\sum_e \int_{\Omega_0^e} \left(\rho_0 \ddot{\boldsymbol{\varphi}}_h - \boldsymbol{\nabla}_0 \cdot \boldsymbol{P}_h\right) \cdot \delta\boldsymbol{\varphi}_h dV \quad = \sum_e \int_{\Omega_0^e} \rho_0 \boldsymbol{B} \delta\boldsymbol{\varphi}_h dV \quad \forall \delta\boldsymbol{\varphi}_h \in \mathrm{X}_{\mathrm{hc}}^{k}, \ \ \forall t \in \mathrm{T} \ . \tag{20}$$

Using Eqs. (6) and (19), the divergence theorem applied to this equation leads to finding $\boldsymbol{\varphi}_h \in \mathrm{X}_{\mathrm{h}}^{k}$ and $\boldsymbol{P}_h \in \mathrm{S}_{\mathrm{h}}^{k}$ such that

$$\begin{aligned} & \sum_e \int_{\Omega_0^e} \left(\rho_0 \ddot{\boldsymbol{\varphi}}_h \cdot \delta\boldsymbol{\varphi}_h + \boldsymbol{P}_h : \boldsymbol{\nabla}_0 \delta\boldsymbol{\varphi}_h\right) dV - \sum_e \int_{\partial_I \Omega_0^e} \boldsymbol{N} \cdot \boldsymbol{P}_h \cdot \delta\boldsymbol{\varphi}_h dS = \\ & \sum_e \int_{\partial_N \Omega_0^e} \bar{\boldsymbol{T}} \cdot \delta\boldsymbol{\varphi}_h dS + \sum_e \int_{\Omega_0^e} \rho_0 \boldsymbol{B} \cdot \delta\boldsymbol{\varphi}_h dV \ \ \forall \delta\boldsymbol{\varphi}_h \in \mathrm{X}_{\mathrm{hc}}^{k}, \ \ \forall t \in \mathrm{T} \ . \end{aligned} \tag{21}$$

In this last equation, the term on the interior boundary $\partial_I \Omega_0^e$ involves fields that are discontinuous and can take two distinct values on opposite sides of this surface. In order to describe discontinuous fields across element boundaries, the jump $[\![\bullet]\!]$ and mean $\langle\bullet\rangle$ operators defined on the space of the trace of functions which can possibly adopt multiple values on the interior boundary $\mathrm{TR}(\partial_I B_{0h}) = \prod_{e=1}^{E} \left(\mathrm{L}^2\left(\partial_I \Omega_0^e\right) \right)$ and defined by

$$[\![\bullet]\!] \, , \ \langle\bullet\rangle \ : \ \left[\mathrm{TR}(\partial_I B_{0h})\right]^{1 \text{ or } 2} \rightarrow \left[\mathrm{L}^2\left(\partial_I B_{0h}\right)\right]^{1 \text{ or } 2} : \ \ [\![\bullet]\!] = \bullet^+ - \bullet^- , \ \langle\bullet\rangle = \frac{1}{2}\left[\bullet^+ + \bullet^-\right] , \tag{22}$$

are introduced. In these expressions,

$$\bullet^{\pm} = \lim_{\varepsilon \rightarrow 0_+} \bullet\left(\boldsymbol{X} \pm \varepsilon \boldsymbol{N}^-\right) \quad \forall \quad \boldsymbol{X} \in \partial_I B_{0h} \ , \tag{23}$$

the bullet represents a generic field, and $\boldsymbol{N}^-$ is conventionally defined as the reference outward unit normal to $\partial\Omega_0^e$. Although the outward unit normal of the considered element is unique, superscript $-$ is used to refer to the element on the $-$ sign of the boundary in order to avoid any confusion when the whole mesh is considered. The defining characteristic of discontinuous Galerkin methods is that the discrete fields $\boldsymbol{\varphi}_h$, $\delta\boldsymbol{\varphi}_h$, and $\boldsymbol{P}_h$ may have finite jumps on $\partial_I B_{0h}$. The main idea of the discontinuous Galerkin method is to address the contribution of the

interelement discontinuity terms by introducing a numerical flux $\boldsymbol{h}\left(\boldsymbol{P}_h^+, \boldsymbol{P}_h^-, \boldsymbol{N}^-\right)$ dependent on the limit values on the surface in the neighboring elements, such that

$$\sum_e \int_{\partial_I \Omega_0^e} \delta\boldsymbol{\varphi}_h \cdot \boldsymbol{P}_h \cdot \boldsymbol{N} dS \rightarrow -\int_{\partial_I B_{0h}} [\![\delta\boldsymbol{\varphi}_h]\!] \cdot \boldsymbol{h}\left(\boldsymbol{P}_h^-, \boldsymbol{P}_h^+, \boldsymbol{N}^-\right) dS \,. \tag{24}$$

Although there is, in principle, significant freedom in the choice of $\boldsymbol{h}$, a consistent formulation requires

$$\boldsymbol{h}\left(\boldsymbol{P}, \boldsymbol{P}, \boldsymbol{N}\right) = \boldsymbol{P}\cdot\boldsymbol{N} \text{ and } \boldsymbol{h}\left(\boldsymbol{P}_h^-, \boldsymbol{P}_h^+, \boldsymbol{N}^-\right) = -\boldsymbol{h}\left(\boldsymbol{P}_h^+, \boldsymbol{P}_h^-, \boldsymbol{N}^+\right) \,, \tag{25}$$

where $\boldsymbol{P}$ is the exact solution. The boundary term can be rewritten using (22) and (23), as

$$\begin{aligned} &\sum_e \int_{\partial_I \Omega_0^e} \delta\boldsymbol{\varphi}_h \cdot \boldsymbol{P}_h \cdot \boldsymbol{N} dS = -\int_{\partial_I B_{0h}} [\![\delta\boldsymbol{\varphi}_h \cdot \boldsymbol{P}_h]\!] \cdot \boldsymbol{N}^- dS \\ &= -\int_{\partial_I B_{0h}} [\![\delta\boldsymbol{\varphi}_h]\!] \cdot \langle \boldsymbol{P}_h \rangle \cdot \boldsymbol{N}^- dS - \int_{\partial_I B_{0h}} \langle \delta\boldsymbol{\varphi}_h \rangle \cdot [\![\boldsymbol{P}_h]\!] \cdot \boldsymbol{N}^- dS \,. \end{aligned} \tag{26}$$

Comparing this relation with Eq. (24), an obvious choice for $\boldsymbol{h}$ is

$$\boldsymbol{h}\left(\boldsymbol{P}_h^-, \boldsymbol{P}_h^+, \boldsymbol{N}^-\right) \;=\; \langle \boldsymbol{P}_h \rangle \cdot \boldsymbol{N}^- \,. \tag{27}$$

The last term of Eq. (26) is not considered because only compatibility of the displacements needs to be enforced. This form of the numerical flux was proposed by Bassi and Rebay [18] in the first discontinuous Galerkin contribution concerning elliptic equations. Other forms of the numerical flux are possible. The average flux was also naturally obtained from a functional in [9]. We refer to the work of Arnold *et al.* [19] and to the new framework proposed by Brezzi *et al.* [20] for a complete discussion on numerical fluxes for space-discontinuous Galerkin discretizations of the elliptic scalar equation. With the choice of average numerical flux (27), the weak formulation (20) simplifies to finding $\boldsymbol{\varphi}_h \in \mathrm{X}_{\mathrm{h}}^k$ and $\boldsymbol{P}_h \in \mathrm{S}_{\mathrm{h}}^k$ such that

$$\begin{aligned} &\int_{B_{0h}} \left(\rho_0 \ddot{\boldsymbol{\varphi}}_h \cdot \delta\boldsymbol{\varphi}_h + \boldsymbol{P}_h : \boldsymbol{\nabla}_0 \delta\boldsymbol{\varphi}_h\right) dV + \int_{\partial_I B_{0h}} [\![\delta\boldsymbol{\varphi}_h]\!] \cdot \langle \boldsymbol{P}_h \rangle \cdot \boldsymbol{N}^- dS = \int_{B_{0h}} \rho_0 \boldsymbol{B} \cdot \delta\boldsymbol{\varphi}_h dV \\ &\qquad + \int_{\partial_N B_{0h}} \delta\boldsymbol{\varphi}_h \cdot \bar{\boldsymbol{T}} dS \quad \forall \delta\boldsymbol{\varphi}_h \in \mathrm{X}_{\mathrm{hc}}^k, \quad \forall t \in \mathrm{T} \,. \end{aligned} \tag{28}$$

In the present formulation, it will be assumed that the constitutive law is enforced strongly from the deformation gradient. *I.e.*, that the deformation gradient used to compute the stress tensor from Eq. (74) is directly computed from the compatible deformation gradient $\boldsymbol{F}_h = \boldsymbol{\nabla}_0 \boldsymbol{\varphi}_h$. In addition, displacement compatibility must be enforced weakly, which also ensures numerical stability. To this end, the compatibility equation $\boldsymbol{\varphi}_h^- - \boldsymbol{\varphi}_h^+ = 0$ on $\partial_I B_{0h}$ is enforced through a (sufficiently large) quadratic stabilization term in $[\![\boldsymbol{\varphi}_h]\!]$, $[\![\delta\boldsymbol{\varphi}_h]\!]$. Whereas in scalar problems this can be achieved by simply adding a term proportional to the scalar product $[\![\boldsymbol{\varphi}_h]\!] \cdot [\![\delta\boldsymbol{\varphi}_h]\!]$, an appropriate term in the context of non-linear mechanics must be proportional to $[\![\boldsymbol{\varphi}_h]\!] \otimes \boldsymbol{N}^- : \mathbb{C} : [\![\delta\boldsymbol{\varphi}_h]\!] \otimes \boldsymbol{N}^-$, where $\mathbb{C} = \frac{\partial \boldsymbol{P}}{\partial \boldsymbol{F}}$ is the tangent material moduli. In this way, general displacement jumps are stabilized in the numerical solution, and the influence of material relations in the presence of large displacements is properly considered. The final formulation of the problem consists of finding $\boldsymbol{\varphi}_h \in \mathrm{X}_{\mathrm{h}}^k$ such that

$$\begin{aligned} &\int_{B_{0h}} \rho_0 \ddot{\boldsymbol{\varphi}}_h \cdot \delta\boldsymbol{\varphi}_h + \boldsymbol{P}_h : \boldsymbol{\nabla}_0 \delta\boldsymbol{\varphi}_h dV + \int_{\partial_I B_{0h}} [\![\delta\boldsymbol{\varphi}_h]\!] \cdot \langle \boldsymbol{P}_h \rangle \cdot \boldsymbol{N}^- dS + \\ &\int_{\partial_I B_{0h}} [\![\delta\boldsymbol{\varphi}_h]\!] \otimes \boldsymbol{N}^- : \left\langle \tfrac{\beta}{h_{\mathrm{s}}} \mathbb{C} \right\rangle : [\![\boldsymbol{\varphi}_h]\!] \otimes \boldsymbol{N}^- dS = \\ &\int_{B_{0h}} \rho_0 \boldsymbol{B} \cdot \delta\boldsymbol{\varphi}_h dV + \int_{\partial_N B_{0h}} \delta\boldsymbol{\varphi}_h \cdot \bar{\boldsymbol{T}} dS \quad \forall \delta\boldsymbol{\varphi}_h \in \mathrm{X}_{\mathrm{hc}}^k, \quad \forall t \in \mathrm{T} \,, \end{aligned} \tag{29}$$

where h_s is the element size and $\beta > 0$ is the stabilization parameter. This approach to the stabilization of the discontinuous Galerkin formulation is similar to the so-called Interior Penalty method [21] in which β plays the role of a penalty parameter, but without the symmetrization term. As explained in [9, 22] for the case of non-linear elastostatics, the formulation could be extended to a symmetric method by adding the symmetrization term $\int_{\partial_I B_{0h}} [\![\boldsymbol{\varphi}_h]\!] \cdot \langle \mathbb{C} : \nabla_0 \delta\boldsymbol{\varphi}_h \rangle \cdot \boldsymbol{N}^- dS$ to the interface terms of Eq. (29), where $\mathbb{C} = \frac{\partial \boldsymbol{P}_h}{\partial \boldsymbol{F}_h}$ are the tangent moduli. This symmetric method has the advantage of having an optimal convergence rate in the L^2-norm for linear problems. However, it also leads to a more involved and computationally-costly parallel implementation since the symmetric interface term results in forces on all the nodes of the bulk elements adjacent to the interface elements.

In the presence of plasticity, only the elastic tangent moduli are considered in the stabilization term:

$$\mathbb{C} = \frac{\partial \boldsymbol{P}_h}{\partial \boldsymbol{F}_h^{\boldsymbol{e}}} \,, \tag{30}$$

as in the limit of perfectly-plastic material the use of the elasto-plastic moduli would lead to a vanishing contribution to stabilizing the DG scheme. The static forces resulting from the weak discontinuous Galerkin formulation (29) are identical to the ones obtained from the three-field Hu-Washizu-de Veubeke formulation for non-linear elasticity [9]. Consequently the consistency and stability of the method, as demonstrated in this reference, apply without modification.

2.2. Finite element discretization

The weak formulation of the dynamics problem (29) is taken as a basis for finite element discretization. To this end, the deformation mapping, its first variation and the material acceleration field are respectively approximated by the interpolations

$$\boldsymbol{\varphi}_h(\boldsymbol{X}) = N_a(\boldsymbol{X})\,\boldsymbol{x}_a \,, \tag{31}$$

$$\delta\boldsymbol{\varphi}_h(\boldsymbol{X}) = N_a(\boldsymbol{X})\,\delta\boldsymbol{x}_a \,, \tag{32}$$

$$\ddot{\boldsymbol{\varphi}}_h(\boldsymbol{X}) = N_a(\boldsymbol{X})\,\ddot{\boldsymbol{x}}_a \,, \tag{33}$$

where N_a is the conventional shape function corresponding to node $a \in [1, N]$, N being the number of nodes. Similarly, the deformation gradient is approximated by

$$\boldsymbol{F}_h(\boldsymbol{X}) = \boldsymbol{\nabla}_0 N_a(\boldsymbol{X})\,\boldsymbol{x}_a \,. \tag{34}$$

In the three-dimensional calculations conducted in this paper, we adopt quadratic ten-node tetrahedral elements. The inertial, internal and external forces then follow directly from (29) as

$$\boldsymbol{M}_{ab}\ddot{\boldsymbol{x}}_b = \int_{B_{0h}} \rho_0 N_a N_b dV \;\; \ddot{\boldsymbol{x}}_b \,, \tag{35}$$

$$\boldsymbol{f}_{\mathrm{int}\,a} = \int_{B_{0h}} \boldsymbol{P}_h : \boldsymbol{\nabla}_0 N_a dV \,, \tag{36}$$

$$\boldsymbol{f}_{\mathrm{ext}\,a} = \int_{B_{0h}} \rho_0 \boldsymbol{B} N_a dV + \int_{\partial_N B_{0h}} \bar{\boldsymbol{T}} N_a dS \,, \tag{37}$$

where $\boldsymbol{M}_{ab}$ is the mass matrix. The interelement consistency and stabilization forces arising

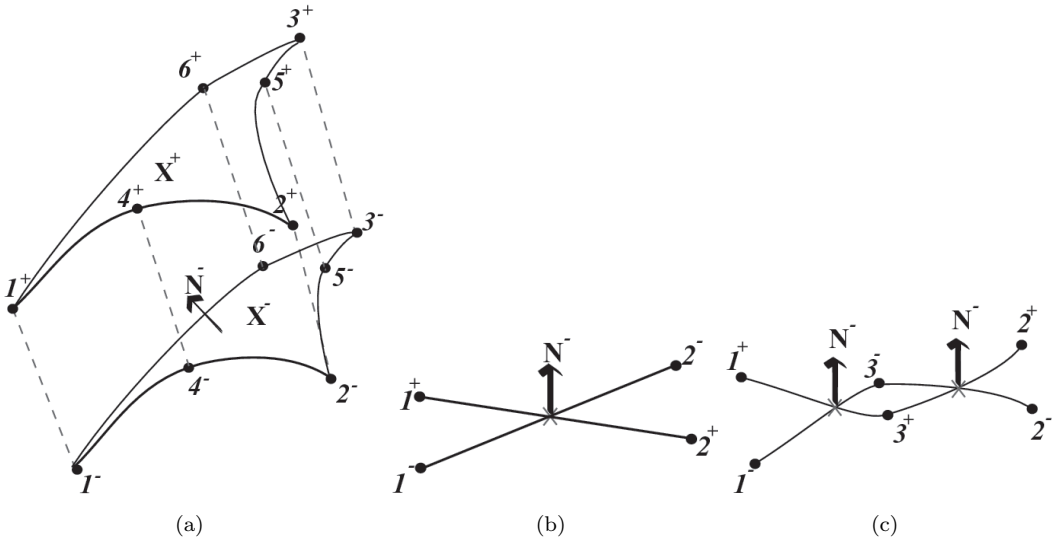

Figure 1. Interface element: (a) illustration of the interface element between two quadratic tetrahedra, (b-c) illustration of a spurious penetration mode between two respectively, linear and quadratic 2D-elements. Crosses represent the Gauss point where the computed jump is equal to zero.

from the discontinuous Galerkin formulation are evaluated from the jump approximations

$$[\![\boldsymbol{\varphi}_h]\!] = N_a \left[\boldsymbol{x}_a^+ - \boldsymbol{x}_a^-\right] \ , \tag{38}$$

$$[\![\delta\boldsymbol{\varphi}_h]\!] = N_a \left[\delta\boldsymbol{x}_a^+ - \delta\boldsymbol{x}_a^-\right] \ , \tag{39}$$

where superscripts + and - refer to the boundaries of the two elements sharing the same interface. When interpolations (38)-(39) are inserted in (29), the expression for the interface forces becomes

$$\boldsymbol{f}_{\mathrm{i}a}^{\pm} \ = \ \pm\int_{\partial_I B_{0h}} \langle \boldsymbol{P}_h \rangle \cdot \boldsymbol{N}^- N_a dS \pm \int_{\partial_I B_{0h}} \left[\left\langle \frac{\beta}{h_{\mathrm{s}}} \mathbb{C} \right\rangle : [\![\boldsymbol{x}_b]\!] \otimes \boldsymbol{N}^- \right] \cdot \boldsymbol{N}^- N_a N_b dS \ , \tag{40}$$

where $[\![\boldsymbol{x}_a]\!] = \boldsymbol{x}_a^+ - \boldsymbol{x}_a^-$ are the jumps in the deformed nodal coordinates. In [9] an implementation of the interface forces (40) in terms of an interface element as illustrated in Figure 1a was proposed. The average Piola-Kirchhoff stresses and elastic Lagrangian tangent moduli in Eq. (30) are computed by extrapolation from their values on the Gauss points of the adjacent elements to the interface element nodes. Higher order quadrature is required to integrate the interelement forces in order to avoid spurious penetration modes; see Figures 1a-b. In calculations, we use 6-point Gauss quadrature. An alternative implementation of a similar discontinuous Galerkin formulation based on a modification of the deformation gradients using the lifting operators has been proposed by Ten Eyck and Lew [8]. The relation between the lifting operator and the inter-element forces has been discussed at length by the authors in [9]. In the present context, the interface elements approach is appealing because it provides a natural framework for modeling fracture via a cohesive theory. By virtue of Eqs. (35-37) and

(40), the finite element approximation of the weak problem (29) results in the semi-discrete system on non-linear ordinary differential equations

$$\boldsymbol{M}_{ab}\ddot{\boldsymbol{x}}_b + \boldsymbol{f}_{\mathrm{int}\,a}\left(\boldsymbol{x}\right) + \boldsymbol{f}_{\mathrm{i}a}\left(\boldsymbol{x}\right) = \boldsymbol{f}_{\mathrm{ext}\,a}, \quad \forall t \in \mathrm{T}\ , \tag{41}$$

$$\boldsymbol{x}_a\left(t=0\right) = \boldsymbol{X}_{0a}\ , \tag{42}$$

$$\dot{\boldsymbol{x}}_a\left(t=0\right) = \boldsymbol{v}_{0a}\ , \tag{43}$$

where $\boldsymbol{x}_0$ are the undeformed nodal coordinates and $\boldsymbol{v}_0$ are the initial nodal velocities.

3. EXPLICIT TIME INTEGRATION

The objective of this paper is to develop scalable algorithms for fast dynamics problems enjoying the properties of discontinuous Galerkin formulations. For this reason, attention is restricted to explicit time integration of the dynamics equations (41). The conventional second-order central-difference scheme [23] with mass lumping is adopted. For completeness, the algorithm is briefly summarized. The integration is accomplished via an incremental solution procedure in which the time interval of interest T is discretized into n^f time steps such that $\mathrm{T} = \bigcup_{n=0}^{n=n^f-1}\left[t^n, t^{n+1}\right]$ and $\triangle t = t^{n+1} - t^n$ is the time step size. Knowing the solution at configuration n, the solution at configuration $n+1$ is given by the expressions

$$\boldsymbol{x}_a^{n+1} = \boldsymbol{x}_a^n + \triangle t\,\dot{\boldsymbol{x}}_a^n + \frac{\triangle t^2}{2}\ddot{\boldsymbol{x}}_a^n\ , \tag{44}$$

$$\dot{\boldsymbol{x}}_a^{n+1} = \dot{\boldsymbol{x}}_a^n + \frac{\triangle t}{2}\left(\ddot{\boldsymbol{x}}_a^n + \ddot{\boldsymbol{x}}_a^{n+1}\right)\ , \tag{45}$$

$$\boldsymbol{M}_{ab}\ddot{\boldsymbol{x}}_b^{n+1} = \left[\boldsymbol{f}_{\mathrm{ext}} - \boldsymbol{f}_{\mathrm{int}} - \boldsymbol{f}_{\mathrm{i}}\right]_a^{n+1}\ , \tag{46}$$

for each node a. This time-stepping scheme can also be rewritten in the more succinct form

$$\boldsymbol{x}_a^{n+1} = \boldsymbol{x}_a^n + \triangle t\,\dot{\boldsymbol{x}}_a^{n+\frac{1}{2}}\ , \tag{47}$$

$$\dot{\boldsymbol{x}}_a^{n+\frac{1}{2}} = \dot{\boldsymbol{x}}_a^{n-\frac{1}{2}} + \triangle t\ddot{\boldsymbol{x}}_a^n\ , \tag{48}$$

$$\boldsymbol{M}_{ab}\ddot{\boldsymbol{x}}_b^{n+1} = \left[\boldsymbol{f}_{\mathrm{ext}} - \boldsymbol{f}_{\mathrm{int}} - \boldsymbol{f}_{\mathrm{i}}\right]_a^{n+1}\ , \tag{49}$$

where the mid-time velocity $\dot{\boldsymbol{x}}_a^{n+\frac{1}{2}}$ is equal to $\dot{\boldsymbol{x}}_a^{n+1} - \frac{\triangle t}{2}\ddot{\boldsymbol{x}}_a^{n+1}$. The evaluation of the Piola-Kirchhoff stress at configuration $n+1$ follows from the integration of the constitutive model which is based on the so-called variational updates, section 2 and appendix I. The space-discontinuous Galerkin formulation imposes an additional time-stability restriction beyond the usual condition

$$\triangle t \leq \triangle t_{\mathrm{crit}} = \frac{l}{c}\ , \tag{50}$$

in the conventional continuous Galerkin approach [24], where l is the smallest characteristic mesh element size and c is the sound speed of the material. In what follows, the implications of the space-discontinuous Galerkin formulation on the time integration stability are analyzed, and a new expression for the critical time step $\triangle t_{\mathrm{crit}}$ is derived. The stability analysis is based on the linearized system [23], in which case the residual forces may be written as

$$\left[\boldsymbol{f}_{\mathrm{int}} + \boldsymbol{f}_{\mathrm{i}} - \boldsymbol{f}_{\mathrm{ext}}\right]_a = \boldsymbol{K}_{ab}\boldsymbol{x}_b\ , \tag{51}$$

where $\boldsymbol{K}$ is the stiffness matrix. Then, Eqs. (44-46) may be rewritten as

$$\boldsymbol{M}_{ab}\left[\frac{\boldsymbol{x}_b^{n+2}-2\boldsymbol{x}_b^{n+1}+\boldsymbol{x}_b^{n}}{\triangle t^2}\right] = \boldsymbol{K}_{ab}\boldsymbol{x}_b^{n+1}\ . \tag{52}$$

Since both the stiffness and the mass matrix are semi-positive definite, there are N_{dof} linearly independent eigenvectors Φ_j and N_{dof} positive eigenvalues λ_j, where N_{dof} is the number of degrees of freedom. These eigenvectors and eigenvalues verify

$$\lambda_j \boldsymbol{M}\Phi_j = \boldsymbol{K}\Phi_j \ \ \forall j \in [1, N_{\text{dof}}]\ . \tag{53}$$

If the unknown field in the base of the eigenvectors is represented by ξ, with $\boldsymbol{x} = \sum_j \xi_j \Phi_j$, Eq. (52) becomes

$$\sum_j \left[\boldsymbol{M}\left[\frac{\xi_j^{n+2}-2\xi_j^{n+1}+\xi_j^{n}}{\triangle t^2}\right]\Phi_j + \boldsymbol{M}\lambda_j\xi_j^{n+1}\Phi_j\right] = 0\ , \tag{54}$$

which decomposes mode by mode as

$$\left[\frac{\xi_j^{n+2}-2\xi_j^{n+1}+\xi_j^{n}}{\triangle t^2}\right] + \lambda_j\xi_j^{n+1} = 0 \ \ \forall j \in [0, N_{\text{dof}}]\ , \tag{55}$$

since the eigenvectors are linearly independent. This set of one-degree-of-freedom equations can be written in matrix form as

$$\begin{pmatrix} \xi_j^{n+2} \\ \xi_j^{n+1} \end{pmatrix} = \begin{pmatrix} 2-\lambda_j\triangle t^2 & -1 \\ 1 & 0 \end{pmatrix}\begin{pmatrix} \xi_j^{n+1} \\ \xi_j^{n} \end{pmatrix} \ \ \forall j \in [1, N_{\text{dof}}]\ . \tag{56}$$

This recursive system is stable and second order accurate providing

$$\triangle t \leq \min_j \frac{2}{\sqrt{\lambda_j}}\ . \tag{57}$$

The critical time step size is therefore determined by the maximum eigenvalue resulting from a linearization of the weak formulation (29), *i.e.*

$$a\left(\boldsymbol{\varphi}_h - \boldsymbol{X}, \delta\boldsymbol{\varphi}_h\right) = b\left(\delta\boldsymbol{\varphi}_h\right)\ . \tag{58}$$

In this expression,

$$\begin{aligned} a\left(\boldsymbol{u}_h, \delta\boldsymbol{\varphi}_h\right) = & \int_{B_h} \rho\ddot{\boldsymbol{u}}_h\cdot\delta\boldsymbol{\varphi}_h dV + \int_{B_h}\boldsymbol{\nabla}\boldsymbol{u}_h : \mathbb{C} : \boldsymbol{\nabla}\delta\boldsymbol{\varphi}_h dV + \\ & \int_{\partial_I B_h}[\![\delta\boldsymbol{\varphi}_h]\!]\otimes\boldsymbol{n}^- : \left\langle\frac{\beta}{h_{\text{s}}}\mathbb{C}\right\rangle : [\![\boldsymbol{u}_h]\!]\otimes\boldsymbol{n}^- dS + \\ & \int_{\partial_I B_h}\boldsymbol{n}^-\cdot\langle\mathbb{C}:\boldsymbol{\nabla}\boldsymbol{u}_h\rangle\cdot[\![\delta\boldsymbol{\varphi}_h]\!]\, dS\ , \end{aligned} \tag{59}$$

$$b\left(\delta\boldsymbol{\varphi}_h\right) = \int_{B_h}\rho\boldsymbol{B}\delta\boldsymbol{\varphi}_h dV + \int_{\partial_N B_h}\bar{\boldsymbol{T}}\cdot\delta\boldsymbol{\varphi}_h dS\ , \tag{60}$$

where $\mathbb{C}$ is the elasticity tensor, $\boldsymbol{n}$ the deformed normal and $\boldsymbol{u}_h = \boldsymbol{\varphi}_h - \boldsymbol{X}$ can be interpreted as a displacement field. For simplicity, the corresponding autonomous unidimensional problem

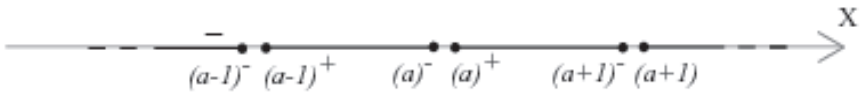

Figure 2. 1D discretization with discontinuous elements.

is considered. To this end, the discretization of a bar of cross-sectional area A, Young modulus E and length l is analyzed, Figure 2. In this system, the characteristic length h_s is obviously equal to the length l. As detailed in Appendix II, the amplification matrix resulting from a first order polynomial approximation is given by

$$\boldsymbol{M}^{-1}\boldsymbol{K} = \frac{E}{\rho l^2}\begin{pmatrix} . & . & . & . & . & . & . & . & . \\ . & [1{+}2\beta] & -1 & 0 & 0 & 0 & 0 & 0 & . \\ . & -1 & [1{+}2\beta] & [1{-}2\beta] & -1 & 0 & 0 & 0 & . \\ . & -1 & [1{-}2\beta] & [1{+}2\beta] & -1 & 0 & 0 & 0 & . \\ . & 0 & 0 & -1 & [1{+}2\beta] & [1{-}2\beta] & -1 & 0 & . \\ . & 0 & 0 & -1 & [1{-}2\beta] & [1{+}2\beta] & -1 & 0 & . \\ . & 0 & 0 & 0 & 0 & -1 & [1{+}2\beta] & [1{-}2\beta] & . \\ . & 0 & 0 & 0 & 0 & -1 & [1{-}2\beta] & [1{+}2\beta] & . \\ . & . & . & . & . & . & . & . & . \end{pmatrix} \begin{matrix} \\ {\scriptstyle (a-2)^+} \\ {\scriptstyle (a-1)^-} \\ {\scriptstyle (a-1)^+} \\ {\scriptstyle (a)^-} \\ {\scriptstyle (a)^+} \\ {\scriptstyle (a+1)^-} \\ {\scriptstyle (a+1)^+} \\ \\ \end{matrix} . \quad (61)$$

Assuming $\beta \geq 1$, as required for stability of the spatial discontinuous Galerkin formulation [9], the maximum eigenvalue of this matrix, is

$$\lambda_{\max} = \frac{E}{\rho l^2} 4\beta \, . \quad (62)$$

It is therefore concluded that the time step restriction (57) of the discontinuous Galerkin method is given by the condition

$$\triangle t \leq \triangle t_{\text{crit}} = \frac{2}{\sqrt{\lambda_{\max}}} = \frac{l}{\sqrt{\beta}}\sqrt{\frac{\rho}{E}} = \frac{l}{\sqrt{\beta} c} \, . \quad (63)$$

As is clear from (63), the discontinuous Galerkin method reduces the critical time step by a factor $\sqrt{\beta}$ when compared to a continuous Galerkin method. In practice [9], a stabilization parameter between 1 and 10 can be chosen in order to ensure both accuracy and stability, and therefore, the additional time restriction is not severe. The explosion of the number of degrees of freedom of the discontinuous Galerkin method and the restriction on the time step size are partly compensated by the high scalability of the method, as shown in the next section. Moreover, Ten Eyck and Lew [8] have shown that the discontinuous Galerkin method can reach the same order of accuracy as the continuous method with coarser meshes.

4. PARALLEL IMPLEMENTATION

In this section, the parallel implementation of the discontinuous Galerkin method developed above is described. The parallelization approach is based on mesh partitioning and message

passing using MPI, as is commonly done for continuous Galerkin finite-element methods, e.g. [25]. This basic approach is extended to compute the interface forces (40) in a scalable way. Figure 3a shows schematically the continuous finite-element discretization $B_{0h} = \bigcup_e \Omega_0^e$ of the

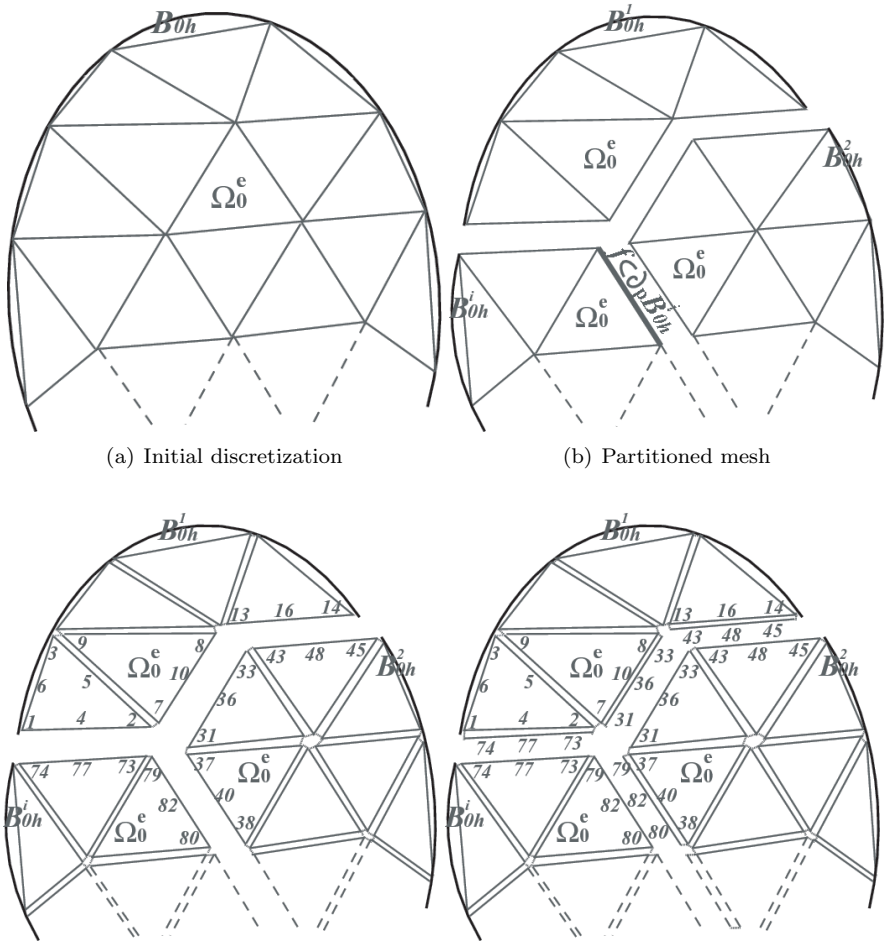

(a) Initial discretization (b) Partitioned mesh

(c) Interfaces inside partitions (d) Interfaces between partitions

Figure 3. Creation of the partitioned discontinuous mesh (schematic).

problem domain B_0. This mesh is partitioned into N_{procs} meshes B_{0h}^i, $i \in [0; N_{\text{procs}} - 1]$ using METIS [26], Figure 3b. At this point, the mid-nodes of the second order elements are introduced. Interface elements are then inserted between two adjacent solid elements of the same processor by duplicating the common nodes (Figure 3c). Then, both the discontinuous Galerkin interface elements at partition boundaries and the necessary communication maps are created. To this end, a unique global identification number (gId) is assigned to all

the nodes of all the partitions, Figure 3c. Next, the element faces belonging to the boundary of each partition are identified and matched to their unique corresponding face in the neighboring partition. The face-matching algorithm consists of the following steps:

for all partitions B^i_{0h}, $i \in [0;\ N_{\text{procs}} - 1]$:
  for all faces $f \subset \partial_p B^i_{0h}$:
    for all neighboring partitions B^j_{0h} of B^i_{0h}, with $j > i$ (to avoid duplication):
      find $g \subset B^j_{0h}$ geometrically matching f
    exchange glds of f and g nodes
    create new interface element $\partial_I \Omega^e_0 \subset B^i_{0h}$ (Figure 3d)
create global-local communication maps at partition boundary nodes using glds.
return

The arbitrary decision to assign the new interface element $\partial_I \Omega^e_0$ to B^i_{0h} can in principle lead to load imbalance. However, the practical consequences of that choice are negligible owing to the small number of interface elements on the boundaries, relative to the overall number of elements in each partition. After the mesh has been partitioned, each processor has only information associated with its local mesh partition. The time integration is achieved following the algorithm described below and summarized in Figure 4. Assuming the solution has been computed up to time t^n, each partition computes its critical time step according to Eq. (63). This value is broadcast to all the processors and the minimum value is selected. Velocities and positions are then computed from Eqs. (44-45) stated in the mid-step velocity form. With these actual positions, the internal forces $\boldsymbol{f}_{\text{int}}$ of the solid elements can be computed from Eq. (36). During the assembly of the internal forces, the elements extrapolate their stresses $\boldsymbol{P}_h$, elastic moduli $\mathbb{C}$ and critical length l to their nodes leading to $\boldsymbol{P}_a$, $\mathbb{C}_a$ and l_a respectively. These values are exchanged with neighboring partitions by using the communication mapping. This results in an exchange of 91 values per node in 3D (the symmetries properties of the tangent moduli can be exploited to reduce the message size). These 91 values are exchanged in one operation. At this point, all of the interface elements, in all of the partitions, know the values needed to compute the interface forces $\boldsymbol{f}_{\text{i}}$ from Eq. (40). The residual force arrays $\boldsymbol{f}_{\text{int}\,a} + \boldsymbol{f}_{\text{i}\,a}$ can then be computed in each partition. The incomplete residuals at the partition boundary nodes require the usual assembly across partitions via a reduction operation. Accelerations are then computed from Eq. (46), and the simulation can proceed to the next time step. As can be seen, the discontinuous Galerkin method involves the exchange between the partitions of 91 more nodal values than does a continuous Galerkin method. However, owing to the significant relative increase of computation inside each partition, the scalability properties are not affected, as discussed in section 5.3.

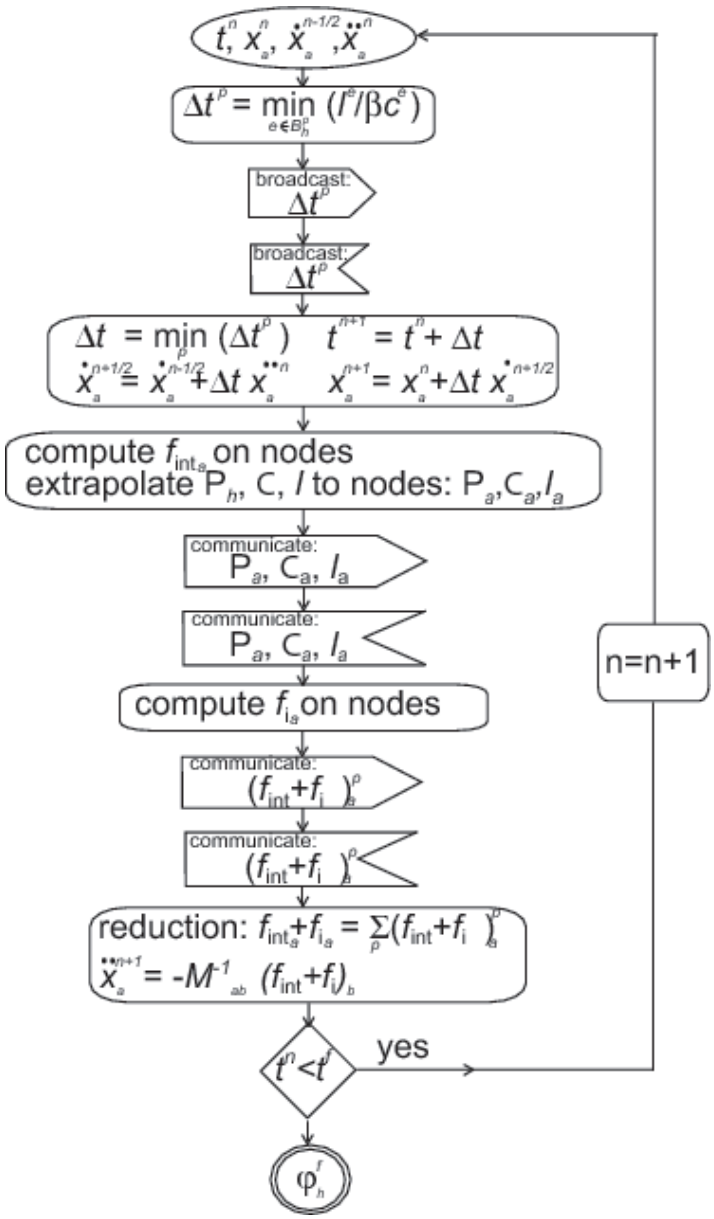

Figure 4. Time integration on one partition.

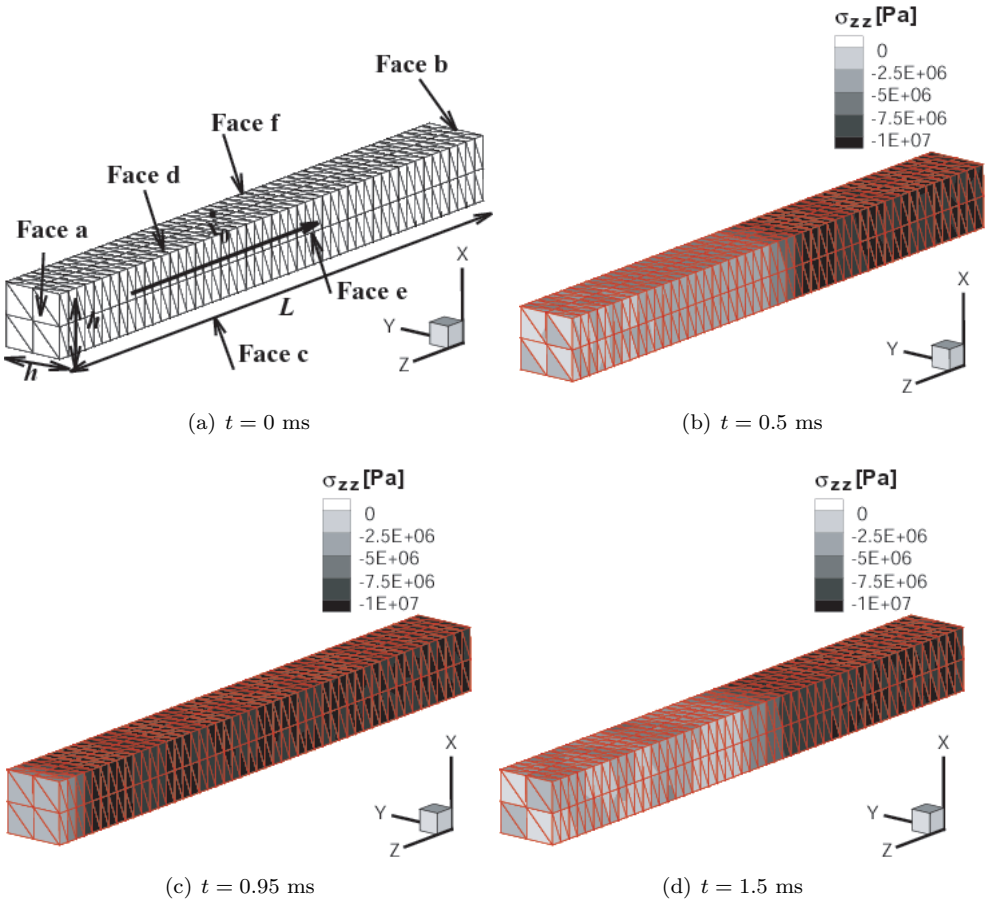

(a) $t = 0$ ms (b) $t = 0.5$ ms

(c) $t = 0.95$ ms (d) $t = 1.5$ ms

Figure 5. Propagation of a uniaxial stress wave in an elastic medium: results shown correspond to $\beta = 1$.

5. NUMERICAL EXAMPLES

In this section, the accuracy, robustness and scalability of the method are demonstrated through of three numerical examples involving wave propagation and high strain-rate plastic deformations.

5.1. Wave propagation

In this example, the propagation of a uniaxial stress wave in an elastic medium is considered, Figure 5a. Faces "c" and "d" are constrained along X, faces "e" and "f" along Y and face "b" along Z. The specimen has an initial velocity $\dot{\boldsymbol{x}}_0$. The material model corresponds to a neo-Hookean model extended to the compressible range without Poisson effect so that the

Table I. Geometric dimensions and material properties used in the simulation of uniaxial stress wave propagation in an elastic medium.

Properties	Values
Length	$L = 1$ m
Height	$h = 0.1$ m
Density	$\rho_0 = 10000$ kg·m^{-3}
Young modulus	$E = 10000$ N·mm^{-2}
Poisson ratio	$\nu = 0$
Sound speed	$c = 1000$ m·s^{-1}
Initial velocity	$\dot{\boldsymbol{x}}_0 = (0; 0; -1$ m·s$^{-1})$

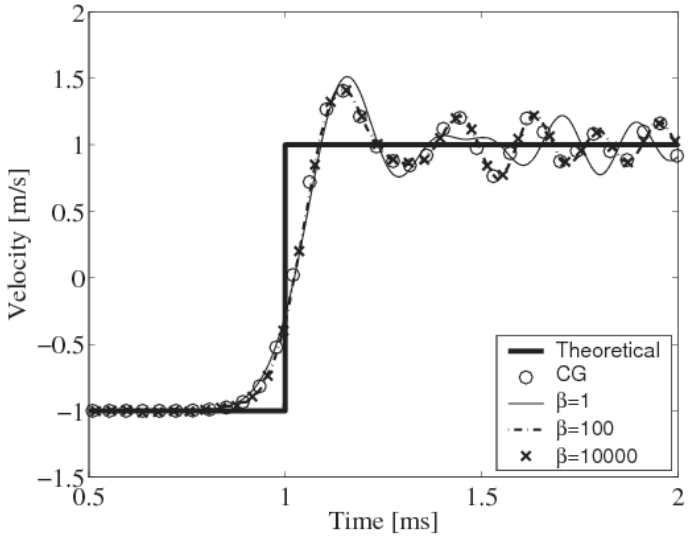

Figure 6. Comparison of the velocity history on face "a" extracted from the simulations using the continuous (CG) and discontinuous (DG) Galerkin methods and the exact velocity history

wave propagation is uniaxial. The strain energy density function is

$$W = \left(\frac{\lambda}{2}\log J - \mu\right)\log J + \frac{\mu}{2}(I_1 - 3)\ , \tag{64}$$

where λ and μ are the Lamé constants, $J = \det(\boldsymbol{F})$ and $I_1 = tr(\boldsymbol{C})$. The geometric dimensions, material properties and initial velocity are given in Table I. At time $t = 0$ ms a compression wave originates in face "b" upon impact and propagates toward face "a" at a speed of 1000 m/s. At time $t = 0.5$ ms, the wave reaches the center of the beam, Figure 5b. At time $t = 1$ ms, this wave reaches face "a", and the beam is fully under compression, Figure 5c. At this point, the wave reflects on the unconstrained end, the velocity of face "a" changes from -1

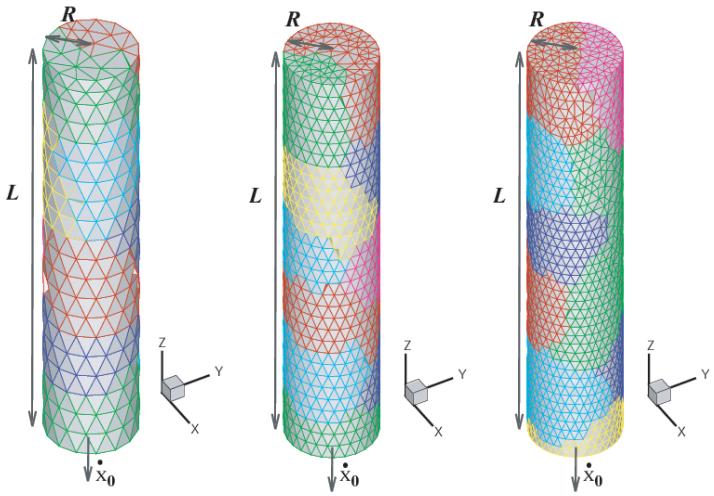

(a) Coarse mesh (b) Fine mesh (c) Finest mesh

Figure 7. Mesh discretizations used in Taylor's impact test simulations.

m/s to 1 m/s and the compressive stress is relieved. At time $t = 1.5$ ms the wave reaches the center of the beam again (Figure 5d).

We compare the discontinuous Galerkin method for β successively taken equal to 1, 100 and 10000, to the continuous Galerkin solution in Figure 6. It can be seen, that the continuous Galerkin methods and the discontinuous Galerkin methods with $\beta > 1$ lead to an essentially identical evolution of the velocity at face "a". The oscillations of the numerical solutions are similar in the continuous and discontinuous spatial discretization and caused by the integration method. For $\beta = 1$, the solution starts to deviate from the continuous Galerkin result, which indicates the onset of instability, as expected due to the low value of the stabilization parameter [9]). It can be concluded that, as long as $\beta \gtrsim 1$, the results provided for the propagation of a uniaxial elastic wave by the discontinuous Galerkin method are consistent with those of the continuous method.

5.2. Taylor's impact test

Taylor's impact test [27], provides a good basis for verification and validation of numerical methods for simulating large, dynamic plastic deformations, as it has been extensively used for characterizing the dynamic response of materials and in numerical studies, e.g. [28]. The test consists of a cylindrical metallic bar impacting a rigid wall at a high velocity. We adopt the specific configuration of the numerical test presented in [29]. In this test, the cylinder material is copper, which is modeled as elasto-plastic with linear isotropic hardening. The impact velocity is 227 m·s^{-1}. The geometric dimensions of the cylinder and the material properties are shown in Table II. Three different meshes consisting of 1216, 6610 and 8238 tetrahedral elements are used in simulations, Figure 7a-c. The simulations were conducted on 10 processors. The mesh partitions distributed to the ten processors used in the simulations are also shown in the

Table II. Geometric dimensions and material properties of cylindrical bar used in Taylor's impact test simulations.

Properties	Values
Radius	$R = 0.0032$ m
Length	$L = 0.0324$ m
Initial velocity	$\dot{\boldsymbol{x}}_0$=(0; 0; -227 m·s^{-1})
Initial density	$\rho_0 = 8930$ kg·m^{-3}
Bulk modulus	$K = 130000$ N·mm^{-2}
Shear modulus	$G = 43333$ N·mm^{-2}
Initial yield stress	$\Sigma_0 = 400$ N·mm^{-2}
Linear hardening	$h = 1004$ N·mm^{-2}

Table III. Results for Taylor's impact test simulation at $t^f = 80\mu s$.

Scheme	Radius	Length	ε^{p}	Maximal jump
DG, coarse, $\beta = 4$	6.811 mm	21.46 mm	2.91	4.1 μm
DG, coarse, $\beta = 16$	6.795 mm	21.45 mm	2.89	1.2 μm
DG, coarse, $\beta = 100$	6.785 mm	21.44 mm	2.84	0.23 μm
CG, coarse	6.791 mm	21.47 mm	2.40	-
DG, fine, $\beta = 4$	7.139 mm	21.46 mm	3.27	2.6 μm
CG, fine	7.130 mm	21.46 mm	2.94	-
DG, finest, $\beta = 4$	7.139 mm	21.46 mm	3.44	-
CG, finest	7.129 mm	21.46 mm	3.30	-
Simo [29]	$6.97mm$	-	-	-

figure. Three simulations were performed using the discontinuous Galerkin method with the coarse mesh and different values of β (4, 16 and 100) in order to compare the method with the continuous Galerkin method. In these simulations, the critical time step size is reduced by a factor of 0.9. The final configurations of the bar and contours of equivalent plastic strain are illustrated in Figure 8. The final radius of the impacting face of the cylinder, cylinder length and maximum equivalent plastic strains are reported in Table III. It can be seen that the radius and length match the continuous Galerkin method with an accuracy within 1%. However, the maximum equivalent plastic strain is larger in the discontinuous Galerkin results. From these simulations, it can be concluded that a stability parameter $\beta = 4$ leads to accurate results with a reduction of the time step only by a factor of 2. It also bears emphasis that in all the discontinuous Galerkin simulations, the jumps remain small, of the order of 1μm, compared to the displacements, which are of the order of 1 mm, Table III. Figures 9 and 10 show the solutions obtained with the finer meshes and $\beta = 4$. The relevant numerical values obtained in these cases have been added to Table III. It can be seen that the maximum plastic strain obtained both with CG and DG methods increases when the mesh size is reduced, as expected. However for any of the given meshes the maximum equivalent plastic strain is always larger with the DG method than with the CG method, thus suggesting that the DG method allows

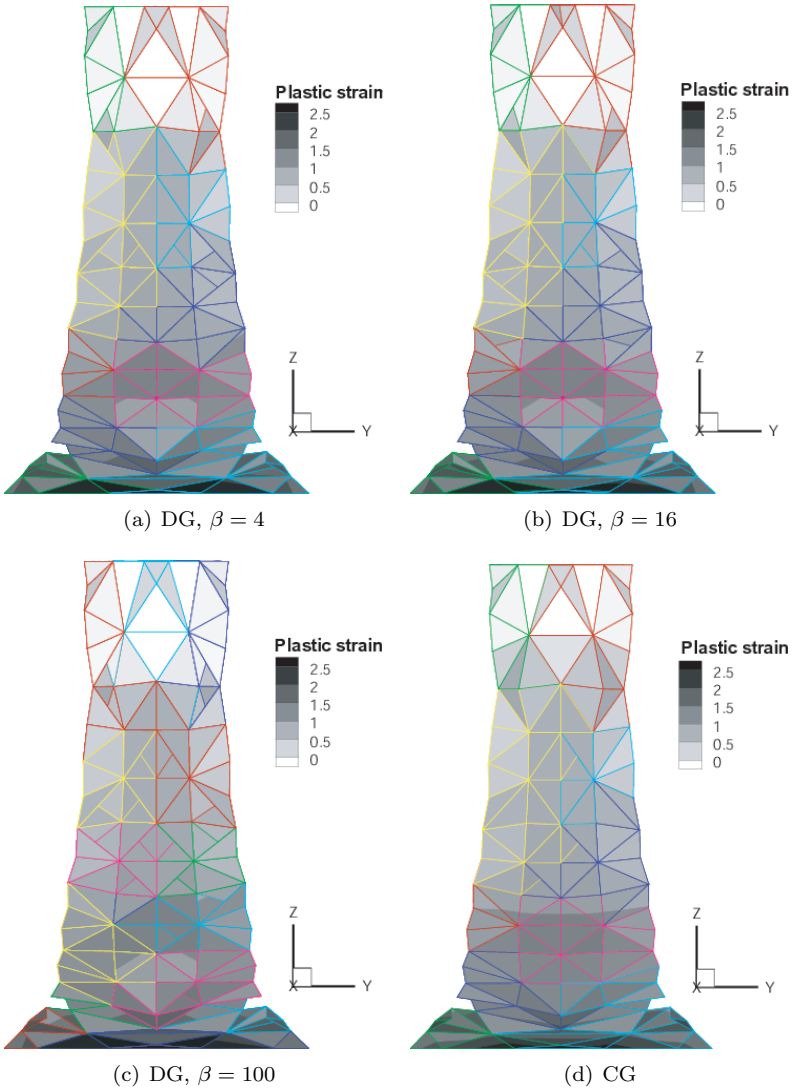

(a) DG, $\beta = 4$ (b) DG, $\beta = 16$

(c) DG, $\beta = 100$ (d) CG

Figure 8. Comparison of Taylor impact test simulations using the DG method with different values of β and continuous Galerkin simulations: Final deformed meshes and contours of equivalent plastic strain corresponding to coarse mesh simulations at time $t^f = 80\mu s$.

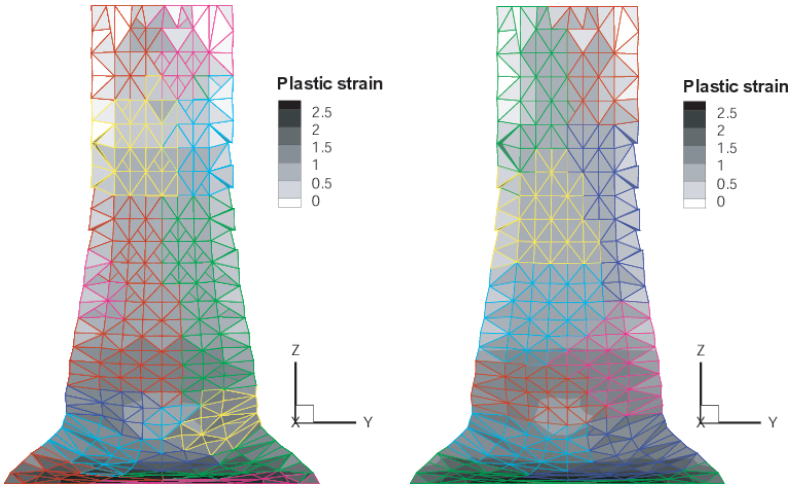

(a) DG, $\beta = 4$ (b) CG

Figure 9. Comparison of Taylor impact test simulations using the DG method with different values of β and continuous Galerkin simulations: Final deformed meshes and contours of equivalent plastic strain corresponding to finer mesh simulations at time $t^f = 80\mu s$.

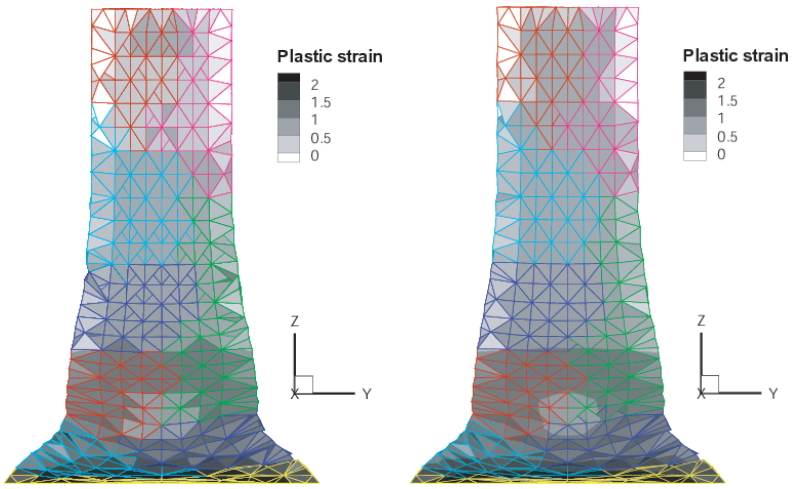

(a) DG, $\beta = 4$ (b) CG

Figure 10. Comparison of Taylor impact test simulations using the DG method with different values of β and continuous Galerkin simulations: Final deformed meshes and contours of equivalent plastic strain corresponding to finest mesh simulations at time $t^f = 80\mu s$.

Table IV. Geometric dimensions and material properties of the elastic rod used in the scalability tests

Properties	Values
Length	$L = 1$ m
Height	$h = 0.1$ m
Density	$\rho_0 = 7800$ kg·m^{-3}
Young modulus	$E = 200000$ N·mm^{-2}
Poisson ratio	$\nu = 0.3$

a better resolution of plastic gradients.

5.3. Scalability

In order to ascertain the potential penalties on scalability incurred by the use of the discontinuous Galerkin method due to additional communication requirements, the following scalability test has been conducted: A uniform tensile test of an elastic rod is simulated using the baseline discretization with 9984 quadratic tetrahedral finite elements, as illustrated in Figure 11. The specimen is clamped on face "b" and uniform displacements are applied on face "a". The material model corresponds to a neo-Hookean model extended to the compressible range, Equation (64). The material parameters and the geometric dimensions of the beam used in calculations are listed in Table IV. Two tests are performed:

(i) Scaled speed-up test (T1): In this case, the number of tetrahedra per processor is kept constant. The initial mesh is used on a single processor run. Subsequently, the problem size and number of processing units (cores) is incremented by a factor of eight and sixty four, respectively, thus maintaining the work load per core. The problem size is increased each time by uniformly subdividing each element into eight tetrahedra.
(ii) Constant size test (T2): In this case, the total number of tetrahedra is kept constant and the number of cores is increased in turn to 4, 8, 16, 32 and 64.

The scalability tests are performed on three different computer cluster configurations:

(i) Opteron-mpich (C1): AMD Opteron nodes, dual processor, dual core, 2.2 Ghz; Compilation done with PathScale 2.3 and mpich 1.2.7; Interconnects: Infiniband; 64-bit architecture;

(ii) Opteron-openmpi (C2): AMD Opteron nodes, dual processor, dual core, 2.2 Ghz; Compilation done with PathScale 2.3 and openmpi 1.0.2; Interconnects: Infiniband; 64-bit architecture;

(iii) IBM Power 5 (C3): 8 Power5 processors/node; 1.9 GHz; Compilation done with IBM AIX 5.3 and openMP; Interconnects: Federation switch, IBM high performance switch.

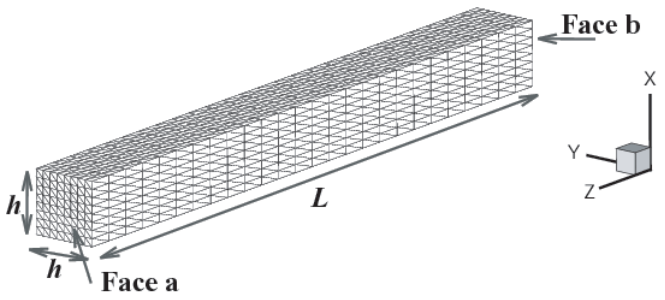

Figure 11. Baseline discretization of the elastic rod used in the scalability test.

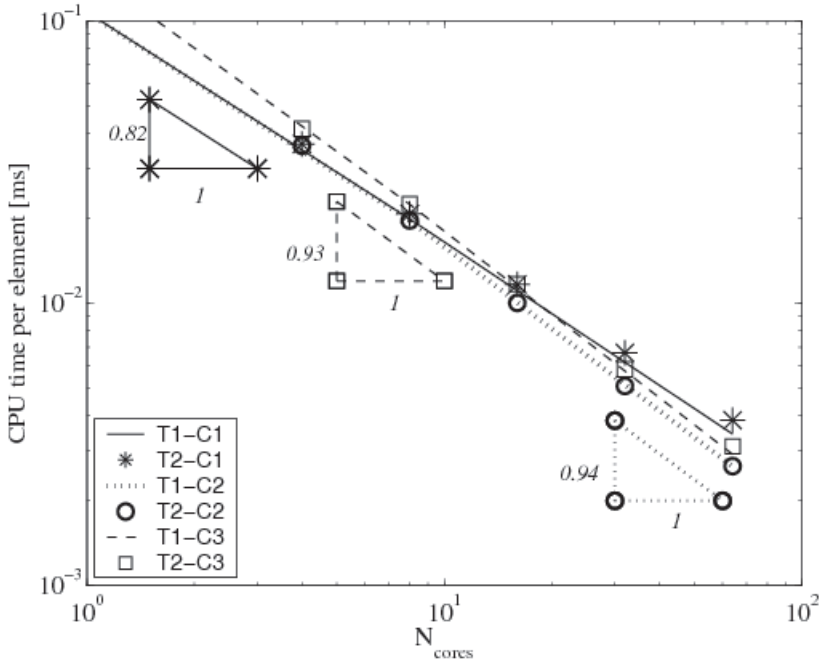

Figure 12. Scaled speed-up (T1) and constant problem size (T2) scalability results: The figure shows the computational time per element needed to compute one time step as a function of the number of cores N_{cores}.

In all these simulations, it was found that the computational time for the slowest processor was only 1.005 times the average computational time for all the processors, which indicates that the waiting time of a processor does not exceed 0.5% of the overall computational time. The time per element needed to compute one time step is reported in Figure 12 as a function of the number of cores for the two different types of tests (T1-T2) and the three machine configurations (C1-C3). The results show speed-up rates between 0.83 and 0.94, which are close to the ideal value of 1. In particular, it is found that the speed-up rates are slightly better than in the same calculations performed with the continuous Galerkin method. For example, test (T2-C2) gives a rate of 0.94 using the discontinuous Galerkin method and 0.90 in the continuous Galerkin case. It can therefore be concluded that, despite the additional communication requirements of the discontinuous Galerkin method, its scalability properties are excellent. This can be explained by the even more significant increase of computational time in each processor associated with the DG approach.

6. CONCLUSIONS

In this paper, a scalable explicit time integration algorithm of a space-discontinuous Galerkin formulation for non-linear dynamics was proposed with focus on problems involving large dynamic plastic deformations. The spatially discontinuous Galerkin formulation involves average numerical fluxes and quadratic stabilization terms which ensure consistency and stability of the spatial discretization. An implementation based on interface elements is described. The numerical fluxes and stabilization terms affect the numerical high-frequency eigenmodes, leading to a modification of the time stability criterion. Time integration stability is shown to require a reduction of the usual critical time step by the square root of the stabilization parameter. However, this reduction is not significant in practice, as a stabilization parameter of order one is sufficient to ensure accurate results. An efficient parallelization of the scheme based on interface elements, is also described. Scalability tests show that the method is highly scalable, which compensates for the increased computation requirements.

Numerical examples involving large dynamic plastic deformations and wave propagation demonstrate the accuracy of the computational method. Results obtained with the discontinuous Galerkin method seem to more accurately capture strain gradients for a given mesh.

ACKNOWLEDGEMENTS

This research was supported by the U.S. Army through the Institute for Soldier Nanotechnologies, under Contract DAAD-19-02-D-0002 with the U.S. Army Research Office. The content does not necessarily reflect the position of the Government, and no official endorsement should be inferred. The authors are indebted to Sharon Brunett for her help with the scalability tests.

REFERENCES

1. A. Lew, P. Neff, D. Sulsky, and M. Ortiz. Optimal BV estimates for a discontinuous Galerkin method for linear elasticity. *Applied Mathematics Research eXpress*, 3:73–106, 2004.

2. P Hansbo and MG Larson. Discontinuous Galerkin methods for incompressible and nearly incompressible elasticity by Nitsche's method. *Computer Methods in Applied Mechanics and Engineering*, 191:1895–1908, 2002.
3. G Engel, K. Garikipati, T.J.R. Hughes, M.G. Larson, L Mazzei, and RL Taylor. Continuous/discontinuous finite element approximations of fourth-order elliptic problems in structural and continuum mechanics with applications to thin beams and plates. *Computer Methods in Applied Mechanics and Engineering*, 191:3669–3750, 2002.
4. S. Güzey, H.K. Stolarski, B. Cockburn, and K.K. Tamma. Design and development of a discontinuous Galerkin method for shells. *Computer Methods in Applied Mechanics and Engineering*, 195:3528–3548, 2006.
5. J. Mergheim, E. Kuhl, and P. Steinmann. A hybrid discontinuous Galerkin/interface method for the computational modelling of failure. *Communication in Numerical Methods in Engineering*, 20:511–519, 2004.
6. G.N. Wells, K. Garikipati, and L. Molari. A discontinuous Galerkin method for strain gradient-dependent damage. *Computer Methods in Applied Mechanics and Engineering*, 193:3633–3645, 2004.
7. L. Molari, G.N. Wells, K. Garikipati, and F. Ubertini. A discontinuous Galerkin method for strain gradient-dependent damage: Study of interpolations and convergence. *Computer Methods in Applied Mechanics and Engineering*, 195:1480–1498, 2006.
8. A. Ten Eyck and A. Lew. Discontinuous Galerkin methods for non-linear elasticity. *International Journal for Numerical Methods in Engineering*, 67:1204–1243, 2006.
9. L. Noels and R. Radovitzky. A general discontinuous Galerkin method for finite hyperelasticity. Formulation and numerical applications. *International Journal for Numerical Methods in Engineering*, 68(1):64–97, 2006.
10. R. Radovitzky and M. Ortiz. Error estimation and adaptive meshing in strongly nonlinear dynamic problems. *Computer Methods in Applied Mechanics and Engineering*, 172:203–240, 1999.
11. M. Ortiz and L. Stainier. The variational formulation of viscoplastic updates. *Computer Methods in Applied Mechanics and Engineering*, 171:419–444, 1999.
12. Ortiz, M. and Pandolfi, A. A variational Cam-clay theory of plasticity. *Computer Methods in Applied Mechanics and Engineering*, 193:2645–2666, 2004.
13. Weinberg, K. and Mota, A. and Ortiz, M. A variational constitutive model for porous metal plasticity. *Computational Mechanics*, 37:142–152, 2006.
14. Weinberg, K. and Ortiz, M. Shock wave induced damage in kidney tissue. *Computational Materials Science*, 32(3–4):588–593, 2005.
15. E. Fancello, J.-P. Ponthot, and L. Stainier. A variational formulation of constitutive models and updates in non-linear finite viscoelasticity. *International Journal for Numerical Methods in Engineering*, 65:1831–1864, 2006.
16. A. Jérusalem, L. Stainier, and R. Radovitzky. A continuum model describing the reverse grain-size dependence of the strength of nanocrystalline metals. *Philosophical Magazine*, 87(17):2541–2559, 2007.
17. Yang, Q. and Stainier, L. and Ortiz, M. A variational formulation of the coupled thermo-mechanical boundary-value problem for general dissipative solids. *Journal of the Mechanics and Physics of Solids*, 54:401–424, 2006.
18. F. Bassi and S. Rebay. A high-order accurate discontinuous finite element method for the numerical solution of the compressible Navier-Stokes equations. *Journal of Computational Physics*, 131:267–279, 1997.
19. D.N. Arnold, F. Brezzi, B. Cockburn, and L.D. Marini. Unified analysis of discontinuous Galerkin methods for elliptic problems. *SIAM Journal of Numerical Analysis*, 39(5):1749–1779, 2002.
20. F. Brezzi, B. Cockburn, L.D. Marini, and E. Tamma, Süli. Stabilization mechanisms in discontinuous Galerkin finite element methods. *Computer Methods in Applied Mechanics and Engineering*, 195:3293–3310, 2006.
21. B. Cockburn. Discontinuous Galerkin methods. *Zeitschrift fuer Angewandte Mathematik und Mechanik*, 83(11):731–754, 2003.
22. L. Noels and R. Radovitzky. Alternative approaches for the derivation of discontinuous galerkin methods for nonlinear mechanics. *Journal of Applied Mechanics*, 2007. accepted.
23. T. Belytschko. *Computational Methods for Transient Analysis*. Elsevier Science, North-Holland, 1983.
24. D.P. Flanagan and T. Belytschko. Eigenvalues and stable timesteps for the uniform strain hexaedron and quadrilateral. *Journal of Applied Mechanics*, 51:35–40, 1981.
25. K.T. Danielson and Namburu R.R. Nonlinear dynamic finite element analysis on parallel computers using FORTRAN 90 and MPI. *Advances in Engineering Software*, 29:179–186, 1998.
26. G. Karypis and V. Kumar. Analysis of multilevel graph partitioning. In Association for Computing Machinery, editor, *Supercomputing*, San Diego, 1995.
27. G. I. Taylor. The use of flat-ended projectiles for determining dynamic yield stress i. theoretical

considerations. *Proc. Royal Soc. London A*, 194:289–299, 1948.
28. G. R. Johnson and T. J. Holmquist. Evaluation of cylinder-impact test data for constitutive models. *Journal of Applied Physics*, 64(8):3901–3910, 1988.
29. J.C. Simo. Algorithms for static dynamic multiplicative plasticity that preserve the classical return mapping schemes of the infinitesimal theory. *Computer Methods in Applied Mechanics and Engineering*, 99:61–112, 1992.

APPENDIX

I. VARIATIONAL UPDATE FOR FINITE PLASTICITY

The material model for large plastic deformation used in this work follows closely the model of Ortiz and Stainier presented in [11]. The starting point is the general framework of section 2, Equations (9-15). The kinetic relations are assumed to derive from an inelastic potential $\Psi(\boldsymbol{Y}, \boldsymbol{Q})$ such that

$$\dot{\boldsymbol{Q}} = \Psi_{,\boldsymbol{Y}}\left(\boldsymbol{Y}, \boldsymbol{Q}\right) , \tag{65}$$

with the dual potential defined by the Legendre transformation

$$\Psi^*\left(\boldsymbol{Q}\right) = \max_{\boldsymbol{Y}} \left(\boldsymbol{Y}\dot{\boldsymbol{Q}} - \Psi(\boldsymbol{Y}, \boldsymbol{Q}) \right) . \tag{66}$$

In these expressions,

$$\boldsymbol{Y} \quad = \quad -A_{,\boldsymbol{Q}}\left(\boldsymbol{F}, \boldsymbol{Q}\right) , \tag{67}$$

are the thermodynamic forces conjugate to $\boldsymbol{Q}$. The free energy density follows in the form

$$A = A(\boldsymbol{F^e}, \varepsilon^{\mathrm{p}}, \boldsymbol{M^p}) , \tag{68}$$

where ε^{p} denotes an equivalent plastic deformation and $\boldsymbol{M^p}$ a plastic flow direction. The plastic flow is directly characterized by an explicit expression of the form (11), with

$$\dot{\boldsymbol{F}}^{\boldsymbol{p}} = \dot{\varepsilon}^{\mathrm{p}} \boldsymbol{M^p} \boldsymbol{F^p} . \tag{69}$$

from where it follows that the complete set of internal variables is reduced to $\boldsymbol{Q} = (\boldsymbol{F^p}, \varepsilon^{\mathrm{p}})$. Correspondingly, the complete set of thermodynamic forces is now $\boldsymbol{Y} = (-\boldsymbol{T}, Y)$, where

$$\boldsymbol{T} \quad = \quad A_{,\boldsymbol{F^p}} \text{ is the backstress and} \tag{70}$$

$$Y \quad = \quad -A_{,\varepsilon^{\mathrm{p}}} \text{ is the overstress.} \tag{71}$$

Relation (70) characterizes the direction of the stress tensor, while relation (71) describes the plastic flow criterion (*e.g.* von Mises yield surface). This previous formulation can be stated in a variational form by defining a functional

$$D\left(\dot{\boldsymbol{F}}, \dot{\varepsilon}^{\mathrm{p}}, \boldsymbol{M^p}\right) = A_{,\boldsymbol{F}} : \dot{\boldsymbol{F}} + Y\dot{\varepsilon}^{\mathrm{p}} + \Psi^*\left(\dot{\varepsilon}^{\mathrm{p}}\right) . \tag{72}$$

Assuming sufficient convexity properties for the physical potentials A and Ψ^*, the stationary point of D corresponds to a minimum [11]. An effective potential D_{eff} is defined at the minimum of D with respect to $\dot{\varepsilon}^{\mathrm{p}}$ and $\boldsymbol{M^p}$:

$$\Delta D_{\mathrm{eff}}\left(\dot{\boldsymbol{F}}\right) = \min_{\dot{\varepsilon}^{\mathrm{p}}, \boldsymbol{M^p}} D\left(\dot{\boldsymbol{F}}, \dot{\varepsilon}^{\mathrm{p}}, \boldsymbol{M^p}\right) . \tag{73}$$

Therefore ΔD_{eff} automatically satisfies (66) and the normality rule. From these definitions, it directly follows that

$$\frac{\partial \Delta D_{\mathrm{eff}}\left(\dot{\boldsymbol{F}}\right)}{\partial \dot{\boldsymbol{F}}} = A_{,\boldsymbol{F}} = \boldsymbol{P} , \tag{74}$$

demonstrating that the Piola stress tensor can be obtained from a variational formulation, even for complex material behavior. In the special case of metals, in which the elastic response is ostensibly independent of the plastic processes, the free energy (68) decomposes additively in the form

$$A = W^{\mathrm{e}}(\boldsymbol{F}\boldsymbol{F}^{p-1}) + W^{\mathrm{p}}(\boldsymbol{F}^{\boldsymbol{p}}, \varepsilon^{\mathrm{p}}) \,. \tag{75}$$

The function W^{e} determines the elastic response of the metal, *e.g.*, upon unloading, whereas the function W^{p} describes the hardening of the material. In the special case of power-law viscosity and hardening it follows that

$$W^{\mathrm{p}} = \frac{nY_0\varepsilon_0^{\mathrm{p}}}{n+1}\left(\frac{\varepsilon^{\mathrm{p}}}{\varepsilon_0^{\mathrm{p}}}\right)^{(n+1)/n} , \tag{76}$$

$$\Psi^* = \begin{cases} \frac{mY_0\dot{\varepsilon}_0^{\mathrm{p}}}{m+1}\left(\frac{\dot{\varepsilon}^{\mathrm{p}}}{\dot{\varepsilon}_0^{\mathrm{p}}}\right)^{\frac{m+1}{m}} , & \dot{\varepsilon}^{\mathrm{p}} \geq 0; \\ \infty & \text{otherwise} , \end{cases} \tag{77}$$

where $\dot{\varepsilon}_0^{\mathrm{p}}$ is a reference strain rate, $\varepsilon_0^{\mathrm{p}}$ is a reference strain, Y_0 is the yield stress, m is the rate-sensitivity exponent and n is the hardening exponent. If the material has a purely elastic behavior, the formulation (74) is reduced to

$$\boldsymbol{P} = \frac{\partial W^{\mathrm{e}}\left(\boldsymbol{F}^T\boldsymbol{F}\right)}{\partial \boldsymbol{F}} , \tag{78}$$

which is the traditional hyperelastic formulation and confirms the consistency of the formulation. The variational constitutive update described above is integrated in time by recourse to an incremental solution procedure. To this end the plastic flow rule (69) is integrated using the exponential mapping

$$\boldsymbol{F}^{\boldsymbol{p}\,n+1} = \exp\left(\left[\varepsilon^{\mathrm{p}\,n+1} - \varepsilon^{\mathrm{p}\,n}\right]\boldsymbol{M}^{\boldsymbol{p}}\right)\boldsymbol{F}^{\boldsymbol{p}\,n} , \tag{79}$$

where $\Delta\varepsilon^{\mathrm{p}} = \varepsilon^{\mathrm{p}\,n+1} - \varepsilon^{\mathrm{p}\,n}$ is the equivalent plastic strain increment and $\boldsymbol{M}^{\boldsymbol{p}}$ is the flow direction. The energy function (72) is redefined as a discrete functional

$$\begin{aligned} \Delta D\left(\boldsymbol{F}^{n+1}, \boldsymbol{F}^{n}, \varepsilon^{\mathrm{p}\,n+1}, \varepsilon^{\mathrm{p}\,n}, \boldsymbol{M}^{\boldsymbol{p}}\right) \equiv A\left(\boldsymbol{F}^{n+1}, \boldsymbol{F}^{\boldsymbol{p}\,n+1}\left(\varepsilon^{\mathrm{p}\,n+1}\right), \varepsilon^{\mathrm{p}\,n+1}\right) - \\ A\left(\boldsymbol{F}^{n}, \boldsymbol{F}^{\boldsymbol{p}\,n}\left(\varepsilon^{\mathrm{p}\,n}\right), \varepsilon^{\mathrm{p}\,n}\right) + \Delta t\Psi^*\left(\frac{\varepsilon^{\mathrm{p}\,n+1} - \varepsilon^{\mathrm{p}\,n}}{\Delta t}\right) . \end{aligned} \tag{80}$$

In this expression, A is the Helmholtz free energy function defined from the elastic energy W^{e} and the plastic dissipation W^{p} by

$$A\left(\boldsymbol{F}, \boldsymbol{F}^{\boldsymbol{p}}, \varepsilon^{\mathrm{p}}\right) \equiv W^{\mathrm{e}}\left(\boldsymbol{F}\boldsymbol{F}^{\boldsymbol{p}\,-1}\right) + W^{\mathrm{p}}\left(\boldsymbol{F}^{\boldsymbol{p}}\left(\varepsilon^{\mathrm{p}}\right), \varepsilon^{\mathrm{p}}\right) . \tag{81}$$

As is common practice in problems involving large plastic deformations in metals, we adopt an elastic model based on the extension of linear elasticity to large deformations using a logarithmic expression of the elastic strain tensor $\boldsymbol{F}^{\boldsymbol{e}\,T}\boldsymbol{F}^{\boldsymbol{e}}$. The incremental version of the effective potential (73) becomes

$$\Delta D_{\mathrm{eff}}\left(\boldsymbol{F}\right) \equiv \min_{\varepsilon^{\mathrm{p}\,n+1}, \boldsymbol{M}^{\boldsymbol{p}}} \Delta D\left(\boldsymbol{F}^{n+1}, \boldsymbol{F}^{n}, \varepsilon^{\mathrm{p}\,n+1}, \varepsilon^{\mathrm{p}\,n}, \boldsymbol{M}^{\boldsymbol{p}}\right) , \tag{82}$$

whereas the discrete stresses arise from (74) and (82) as

$$\boldsymbol{P}^{n+1} = \frac{\partial \Delta D_{\mathrm{eff}}\left(\boldsymbol{F}^{n+1}\right)}{\partial \boldsymbol{F}^{n+1}} = \frac{\partial A\left(\boldsymbol{F}^{n+1}\right)}{\partial \boldsymbol{F}^{n+1}} . \tag{83}$$

II. AMPLIFICATION MATRIX OF THE 1D SYSTEM

Assuming a first order polynomial approximation, the inertial term of Eq. (59) can be rewritten as

$$\int_{B_h} \rho \ddot{\boldsymbol{u}}_h \cdot \delta\boldsymbol{\varphi}_h dV = \sum_a \frac{\rho A l}{6}\left[2\ddot{\boldsymbol{u}}^-_{a+1} + \ddot{\boldsymbol{u}}^+_a\right]\delta\boldsymbol{\varphi}^-_{a+1} + \frac{\rho A l}{6}\left[\ddot{\boldsymbol{u}}^-_{a+1} + 2\ddot{\boldsymbol{u}}^+_a\right]\delta\boldsymbol{\varphi}^+_a \ , \tag{84}$$

where $\boldsymbol{u}^\pm_a$ and $\delta\boldsymbol{\varphi}^\pm_a$ are respectively the displacement and the admissible variation at node $a^\pm$. Using mass lumping, this expression simplifies to

$$\int_{B_h} \rho \ddot{\boldsymbol{u}}_h \cdot \delta\boldsymbol{\varphi}_h dV = \sum_a \frac{\rho A l}{2}\left[\ddot{\boldsymbol{u}}^-_{a+1}\delta\boldsymbol{\varphi}^-_{a+1} + \ddot{\boldsymbol{u}}^+_a\delta\boldsymbol{\varphi}^+_a\right] \ , \tag{85}$$

resulting in the equivalent mass matrix

$$\boldsymbol{M} = \frac{\rho A l}{2}\begin{pmatrix} . & . & . & . & . & . & . & . & . \\ . & 1 & 0 & 0 & 0 & 0 & 0 & 0 & . \\ . & 0 & 1 & 0 & 0 & 0 & 0 & 0 & . \\ . & 0 & 0 & 1 & 0 & 0 & 0 & 0 & . \\ . & 0 & 0 & 0 & 1 & 0 & 0 & 0 & . \\ . & 0 & 0 & 0 & 0 & 1 & 0 & 0 & . \\ . & 0 & 0 & 0 & 0 & 0 & 1 & 0 & . \\ . & 0 & 0 & 0 & 0 & 0 & 0 & 1 & . \\ . & . & . & . & . & . & . & . & . \end{pmatrix} \begin{matrix} \\ (a-2)^+ \\ (a-1)^- \\ (a-1)^+ \\ (a)^- \\ (a)^+ \\ (a+1)^- \\ (a+1)^+ \\ \end{matrix} \ , \tag{86}$$

where the right column gives the node to which the line is related. The volume term of Eq. (59) can be rewritten as

$$\int_{B_h} \boldsymbol{\nabla}\boldsymbol{u}_h : \mathbb{C} : \boldsymbol{\nabla}\delta\boldsymbol{\varphi}_h dV = \sum_a \frac{EA}{l}\left[\boldsymbol{u}^-_{a+1} - \boldsymbol{u}^+_a\right]\left[\delta\boldsymbol{\varphi}^-_{a+1} - \delta\boldsymbol{\varphi}^+_a\right] \ , \tag{87}$$

and the stabilization term as

$$\int_{\partial_I B_h} [\![\delta\boldsymbol{\varphi}_h]\!] \otimes \boldsymbol{n}^- \ : \ \left\langle \frac{\beta}{h_s}\mathbb{C} \right\rangle \ : \ [\![\boldsymbol{u}_h]\!] \otimes \boldsymbol{n}^- dS \ = \ \sum_a \frac{\beta EA}{h_s}\left[\boldsymbol{u}^+_a - \boldsymbol{u}^-_a\right]\left[\delta\boldsymbol{\varphi}^+_a - \delta\boldsymbol{\varphi}^-_a\right] \ . \tag{88}$$

The consistency term of Eq. (59) depends on the average value of a gradient on the interface. On interface a (between nodes a^- and a^+), one has

$$\langle \boldsymbol{\nabla}\boldsymbol{u}_h \rangle_a \ = \ \frac{1}{2l}\left[\boldsymbol{u}^-_a - \boldsymbol{u}^+_{a-1} + \boldsymbol{u}^-_{a+1} - \boldsymbol{u}^+_a\right] \ , \tag{89}$$

leading to

$$\int_{\partial_I B_h} \boldsymbol{n}^- \cdot \langle \mathbb{C} : \boldsymbol{\nabla}\boldsymbol{u}_h \rangle \cdot [\![\delta\boldsymbol{\varphi}_h]\!] \, dS \ = \ \sum_a \frac{EA}{2l}\left[\boldsymbol{u}^-_a - \boldsymbol{u}^+_{a-1} + \boldsymbol{u}^-_{a+1} - \boldsymbol{u}^+_a\right]\left[\delta\boldsymbol{\varphi}^+_a - \delta\boldsymbol{\varphi}^-_a\right] \ . \tag{90}$$

The forces at nodes $a^\pm$ can be derived by extracting the coefficients of $\delta\boldsymbol{\varphi}^\pm_a$ in Eqs. (87), (88) and (90), leading to

$$\frac{l}{EA}\left[\boldsymbol{f}_{\text{int}} + \boldsymbol{f}_{\text{i}}\right]^+_a \ = \ -\frac{1}{2}\boldsymbol{u}^+_{a-1} + \left[\frac{1}{2} - \frac{\beta l}{h_s}\right]\boldsymbol{u}^-_a + \left[\frac{1}{2} + \frac{\beta l}{h_s}\right]\boldsymbol{u}^+_a - \frac{1}{2}\boldsymbol{u}^-_{a+1} \ , \tag{91}$$

$$\frac{l}{EA}\left[\boldsymbol{f}_{\text{int}} + \boldsymbol{f}_{\text{i}}\right]^-_a \ = \ -\frac{1}{2}\boldsymbol{u}^+_{a-1} + \left[\frac{1}{2} + \frac{\beta l}{h_s}\right]\boldsymbol{u}^-_a + \left[\frac{1}{2} - \frac{\beta l}{h_s}\right]\boldsymbol{u}^+_a - \frac{1}{2}\boldsymbol{u}^-_{a+1} \ . \tag{92}$$

If the characteristic length h_s is taken equal to the length l, the stiffness matrix resulting from Eqs. (91)-(92) is

$$\boldsymbol{K} = \frac{EA}{l} \begin{pmatrix} . & . & . & . & . & . & . & . & . \\ . & \left[\frac{1}{2}+\beta\right] & -\frac{1}{2} & 0 & 0 & 0 & 0 & 0 & . \\ . & -\frac{1}{2} & \left[\frac{1}{2}+\beta\right] & \left[\frac{1}{2}-2\beta\right] & \frac{-1}{2} & 0 & 0 & 0 & . \\ . & \frac{-1}{2} & \left[\frac{1}{2}-\beta\right] & \left[\frac{1}{2}+\beta\right] & -\frac{1}{2} & 0 & 0 & 0 & . \\ . & 0 & 0 & -\frac{1}{2} & \left[\frac{1}{2}+\beta\right] & \left[\frac{1}{2}-\beta\right] & \frac{-1}{2} & 0 & . \\ . & 0 & 0 & \frac{-1}{2} & \left[\frac{1}{2}-\beta\right] & \left[\frac{1}{2}+\beta\right] & -\frac{1}{2} & 0 & . \\ . & 0 & 0 & 0 & 0 & -\frac{1}{2} & \left[\frac{1}{2}+\beta\right] & \left[\frac{1}{2}-\beta\right] & . \\ . & 0 & 0 & 0 & 0 & \frac{-1}{2} & \left[\frac{1}{2}-\beta\right] & \left[\frac{1}{2}+\beta\right] & . \\ . & . & . & . & . & . & . & . & . \end{pmatrix} \begin{matrix} \\ {}_{(a-2)^+} \\ {}_{(a-1)^-} \\ {}_{(a-1)^+} \\ {}_{(a)^-} \\ {}_{(a)^+} \\ {}_{(a+1)^-} \\ {}_{(a+1)^+} \\ \\ \end{matrix} . \tag{93}$$

Equations (86) and (93) finally lead to the amplification matrix

$$\boldsymbol{M}^{-1}\boldsymbol{K} = \frac{E}{\rho l^2} \begin{pmatrix} . & . & . & . & . & . & . & . & . \\ . & [1+2\beta] & -1 & 0 & 0 & 0 & 0 & 0 & . \\ . & -1 & [1+2\beta] & [1-2\beta] & -1 & 0 & 0 & 0 & . \\ . & -1 & [1-2\beta] & [1+2\beta] & -1 & 0 & 0 & 0 & . \\ . & 0 & 0 & -1 & [1+2\beta] & [1-2\beta] & -1 & 0 & . \\ . & 0 & 0 & -1 & [1-2\beta] & [1+2\beta] & -1 & 0 & . \\ . & 0 & 0 & 0 & 0 & -1 & [1+2\beta] & [1-2\beta] & . \\ . & 0 & 0 & 0 & 0 & -1 & [1-2\beta] & [1+2\beta] & . \\ . & . & . & . & . & . & . & . & . \end{pmatrix} \begin{matrix} \\ {}_{(a-2)^+} \\ {}_{(a-1)^-} \\ {}_{(a-1)^+} \\ {}_{(a)^-} \\ {}_{(a)^+} \\ {}_{(a+1)^-} \\ {}_{(a+1)^+} \\ \\ \end{matrix} . \tag{94}$$